

Université de Montréal

LHC luminosity measurement with the ATLAS-MPX detectors.

par
Nedaa Asbah

Département de physique
Faculté des arts et des sciences

Mémoire présenté à la Faculté des études supérieures
en vue de l'obtention du grade de Maître ès sciences (M.Sc.)
en physique

Décembre, 2013

© Nedaa Asbah, 2013.

Université de Montréal
Faculté des études supérieures

Ce mémoire intitulé:

LHC luminosity measurement with the ATLAS-MPX detectors.

présenté par:

Nedaa Asbah

a été évalué par un jury composé des personnes suivantes:

Prof. Pierre Bastien,	président-rapporteur
Prof. Claude Leroy,	directeur de recherche
Prof. François Schiettekatte,	membre du jury

Mémoire accepté le: 24 Janvier, 2014

RÉSUMÉ

En opération depuis 2008, l'expérience ATLAS est la plus grande de toutes les expériences au LHC. Les détecteurs ATLAS- MPX (MPX) installés dans ATLAS sont basés sur le détecteur au silicium à pixels Medipix2 qui a été développé par la collaboration Medipix au CERN pour faire de l'imagerie en temps réel. Les détecteurs MPX peuvent être utilisés pour mesurer la luminosité. Ils ont été installés à seize différents endroits dans les zones expérimentale et technique d'ATLAS en 2008. Le réseau MPX a recueilli avec succès des données indépendamment de la chaîne d'enregistrement des données ATLAS de 2008 à 2013. Chaque détecteur MPX fournit des mesures de la luminosité intégrée du LHC. Ce mémoire décrit la méthode d'étalonnage de la luminosité absolue mesurée avec les détecteurs MPX et la performance des détecteurs MPX pour les données de luminosité en 2012. Une constante d'étalonnage de la luminosité a été déterminée. L'étalonnage est basé sur technique de van der Meer (vdM). Cette technique permet la mesure de la taille des deux faisceaux en recouvrement dans le plan vertical et horizontal au point d'interaction d'ATLAS (IP1). La détermination de la luminosité absolue nécessite la connaissance précise de l'intensité des faisceaux et du nombre de trains de particules. Les trois balayages d'étalonnage ont été analysés et les résultats obtenus par les détecteurs MPX ont été comparés aux autres détecteurs d'ATLAS dédiés spécifiquement à la mesure de la luminosité. La luminosité obtenue à partir des balayages vdM a été comparée à la luminosité des collisions proton- proton avant et après les balayages vdM. Le réseau des détecteurs MPX donne des informations fiables pour la détermination de la luminosité de l'expérience ATLAS sur un large intervalle (luminosité de $5 \times 10^{29} \text{cm}^{-2} \text{s}^{-1}$ jusqu'à $7 \times 10^{33} \text{cm}^{-2} \text{s}^{-1}$).

Mots clés:détecteur à pixels ; luminosité ; ATLAS ; LHC.

ABSTRACT

In operation since 2008, the ATLAS experiment is the largest of all the experiments at the LHC. The ATLAS-MPX (MPX) detectors installed in ATLAS are based on the Medipix2 silicon pixelated detector which has been developed by the Medipix Collaboration at CERN to perform real-time imaging. They can be used for luminosity measurements. They were installed at sixteen different positions in the ATLAS cavern at the LHC in 2008. The MPX network successfully collected data independently of the ATLAS data recording chain from 2008 to 2013. Each MPX detector provides measurements of the integrated LHC luminosity. This thesis describes the technique for calibrating the luminosity data and performance of MPX detectors for measuring the luminosity in 2012. The calibration was performed via the van der Meer (vdM) scans technique which allows the measurement of the convolved beam sizes in the vertical and the horizontal planes at the ATLAS interaction point (IP1). The determination of the absolute luminosity requires a precise knowledge of the beam intensities and the number of beam bunches. A luminosity calibration constant was determined. The three calibration scans were analyzed and the results were cross-checked among the MPX detectors and other ATLAS sub-detectors specifically dedicated to luminosity measurement. The luminosity determined from the calibration scans was compared to the luminosity of regular runs before and after the vdM scans. The MPX network gives reliable information for the overall ATLAS luminosity determination over a wide dynamic range (luminosity from $5 \times 10^{29} \text{cm}^{-2} \text{s}^{-1}$ up to $7 \times 10^{33} \text{cm}^{-2} \text{s}^{-1}$).

Keywords: Pixel detector; luminosity; ATLAS; LHC

CONTENTS

RÉSUMÉ	iii
ABSTRACT	iv
CONTENTS	v
LIST OF TABLES	viii
LIST OF FIGURES	ix
LIST OF ABBREVIATIONS	xi
NOTATION	xiii
DEDICATION	xiv
THANKS	xv
CONTRIBUTION	xvi
INTRODUCTION	xvii
CHAPTER 1: THE ATLAS EXPERIMENT AT CERN	1
1.1 ATLAS Experiment	1
1.2 The ATLAS Detector	2
CHAPTER 2: SEMICONDUCTORS AND INTERACTIONS OF PARTICLES WITH MATTER	5
2.1 Fundamentals of semiconductors	5
2.2 Electrical conductivity; mobility	6
2.3 p-n Junction	8
2.4 depletion zone	8

2.5	Passage of Particles Through Matter	10
CHAPTER 3:	THE MEDIPIX2 (MPX) DETECTOR IN ATLAS	12
3.1	Description of the MPX detector	12
3.2	Characterization of tracks with MPX detectors	17
3.3	The MPX network	17
3.4	Modes of operations and pattern track recognition	18
3.5	Neutron detection using the MPX detectors	21
CHAPTER 4:	CONCEPT OF LUMINOSITY	24
4.1	Concept of Luminosity	24
4.2	Luminosity of colliding Gaussian beams	26
4.3	Integrated luminosity	27
4.4	Luminosity calibration scans	28
4.5	Detectors of luminosity in ATLAS	29
CHAPTER 5:	MPX DETECTORS SENSITIVITY TO LHC LUMINOSITY IN 2012	31
5.1	p-p van der Meer luminosity scans	31
5.2	Noisy pixel removal	33
5.3	Converting counts to luminosity	35
5.4	Fitting functions	37
5.5	Time shift	38
5.6	Results for April scan (LHC Fill 2520)	38
5.7	Results for July scan (LHC Fill 2855)	39
5.8	Results for November scan (LHC Fill 3311 and 3316)	46
5.9	Comparison between luminosity obtained during calibration scans and high luminosity runs	49
5.10	Summary of the 2012 vdM luminosity calibration scans	49
Conclusion	53

BIBLIOGRAPHY 55

LIST OF TABLES

3.I	MPX detectors location and position with respect to the ATLAS interaction point IP1	20
5.I	Summary of amplitudes of MPX01 luminosity, BCM luminosity in April vdM scan	42
5.II	Summary of the background measured by MPX01 obtained from single Gaussian plus a constant fit	42
5.III	Summary of Amplitudes of MPX01 luminosity, and BCM luminosity for the July vdM scans	45
5.IV	Summary of the background measured by MPX01 obtained from single Gaussian plus a constant fit	45
5.V	Summary of Amplitudes of MPX01 luminosity, and BCM luminosity for the November vdM scans	46
5.VI	Summary of the background measured by MPX01 obtained from single Gaussian plus a constant fit	49
5.VII	Summary of ratio of the luminosity measured by MPX01 and BCM for high luminosity runs before and after the 2012 vdM scan	51

LIST OF FIGURES

1.1	A computer generated view of a vertical section of the ATLAS detector	4
2.1	Energy band in different solids; insulator, semiconductor, and conductor.	7
2.2	Depletion zone	9
3.1	Picture of a scheme of the bump bonded sensor layer (a), and a picture of a MPX detector with a USB-readout	14
3.2	MPX (Medipix2 in the figure) chipboard	14
3.3	MPX surface plan and block diagram	15
3.4	MPX pixel cell block diagram	15
3.5	Radiation field in ATLAS as seen on the 29 th September 2011 by MPX01	16
3.6	Different pixel shapes generated by various types of particles	17
3.7	The network of MPX detectors in ATLAS	18
3.8	Locations and orientations of MPX detectors with their labels for 12 of the 16 MPX detectors	19
3.9	Background measurement in the ATLAS cavern in 2008 before any collisions period	22
3.10	The MPX sensor covered with neutron converter Layers	23
4.1	Schematic view of a colliding beam interaction	25
4.2	Number of counts measured by MPX01 as a function of time during lead-lead collisions in November 2011	30
4.3	Schematic view of the ATLAS detector with dedicated six detectors of luminosity	30
5.1	van der Meer scans as observed with MPX01 in April	33

5.2	Part of the van der Meer scans as observed with MPX01 detector in July	34
5.3	Part of the van der Meer scans as observed with MPX01 detector in November	34
5.4	A frame taken during the van der Mer scan LHC Fills 3311 and 3316	35
5.5	The number of normalized count rates measured by MPX01 detector during the first horizontal scan in April (LHC Fill 2520) . .	36
5.6	Time history of (a) the MPX01 luminosity and (b) the MPX01/BCM luminosity ratio LHC for Fill 2649	36
5.7	A Single Gaussian distribution	37
5.8	Time shift	39
5.9	Results for April vdM scan	40
5.10	MPX01 hit luminosity vs. BCM luminosity for the second vertical April 2012 vdM scan	41
5.11	Results for July vdM scan	43
5.12	MPX01 hit luminosity vs. BCM luminosity for the sixth vertical July 2012 vdM scan	44
5.13	Results for the November vdM scans	47
5.14	MPX01 hit luminosity vs. BCM luminosity for the second horizontal November 2012 vdM scan	48
5.15	High luminosity run performed on the 18 th of November 2012 . .	50
5.16	Summary of luminosity ratio measured by MPX01 and BCM for the 22 vdM scans performed in 2012 and the luminosity ratio of regular runs before and after the vdM scans	52

LIST OF ABBREVIATIONS

ALFA	Absolute Luminosity For ATLAS
ALICE	A Large Ion Collider Experiment
ATLAS	A Toroidal LHC Apparatus
ASIC	Application- Specific Integrated Circuit
BCM	Beam Conditions Monitor
CB	Conduction Band
CERN	European Organization for Nuclear Research
CMOS	Complementary Metal- Oxide- Semi conductor
CMS	Compact Muon Solenoid
EMC	Electromagnetic Calorimeter
Fcal	Forward calorimeter
HAD	hadronic calorimeter
HETP	High Energy Transfer Particles
HT	High Threshold
IP1	ATLAS interaction point
LAr	Liquid Argon
LETP	Low Energy Transfer Particles
LHC	Large Hadron Collider
LHCb	Large Hadron Collider beauty
LHCf	Large Hadron Collider forward
LT	Lowest Threshold
LUCID	Luminosity measurement using Cerenkov Integrating Detector

MIPs	Minimum Ionizing Particles
MPX	ATLAS-MPX
MoEDAL	Monopole and Exotics Detector At the LHC
SCT	Semi Conductor Tracker
SM	Standard Model
TileCal	Tile Calorimeter
TOF	Time Of Flight
TOT	Time Over Threshold
TOTEM	TOTAL Elastic and diffractive cross section Measurement
TRT	Transition Radiation Tracker
USB	Universal Serial Bus
VB	Valence Band
ZDC	Zero-Degree Calorimeter

NOTATION

CdTe	Cadmium Telluride
eV	electron Volt
GeV	Gigaelectron Volt
keV	kiloelectron Volt
GaAs	Gallium Arsenide
Ge	Germanium
K	kelvin
⁶ LiF	Lithium Floride
meV	millielectron Volt
MeV	Megaelectron Volt
Mg	Magnesium
PE	Polyethylene
Si	Silicium
T	Tesla
TeV	Teraelectron Volt

To my parents

THANKS

“Advance and never halt, for advancing is perfection”... Khalil Gibran

Special thanks to my supervisor Prof. Claude Leroy for his supervision, and confidence in my abilities in the past two years during my MSc studies at the laboratory René- J.-A.-Lévesque. Special thanks to Prof. Stanislav Posipsil for the collaboration with his group and for the great hospitality during my visits to Prague. Thanks to all my colleagues in the medipix collaboration, especially to John Idarraga for his help in the analysis of the data taken with the TIMEPIX detector. Thanks to Prof. Vincent Hedberg and Witold Kozanecki of the luminosity task force group for their help during the analysis. Thanks to Prof. Jean-François Arguin and Prof. Georges Azuelos and all post-doctoral fellows, PhD and MSc students in the ATLAS- Montréal group for their continued support, specially to my colleague Paul.

I would like to thank my family; my dear parents and sisters Nimara and Malvina for their endless love, support, and confidence in me; and my cousins Nathalie, Maroupi and Anwar for their amazing company and support during my stay in Montreal. Many thanks to my aunt Amal and her husband Yusuf for their endless love and hospitality during the past 7 years in Montreal. Special thanks to my aunt Amal for her help in correcting and editing this thesis. Thank you very much.

Thanks also to all my friends all over the world who accompanied me in my life journey up to now. Special thanks to my boyfriend Dominik for his love, confidence in me, and endless support while writing this thesis.

CONTRIBUTION

The analysis presented in this thesis contributed to the luminosity evaluation of the 2012 collision period at the LHC. The luminosity was measured with the MPX detectors, with a special emphasis on the vdM luminosity calibration scans. I analyzed all the calibrations scans using my own analysis codes and I contributed to some figures in the ATLAS- MPX 2012 note that was approved and published by ATLAS in [1].

During my Msc. project, I participated in the characterization studies of a TIMEPIX detector with radioactive sources and proton and alpha particle beams delivered by the Tandem accelerator at University of Montreal. I participated in the data taking and in the data analysis. These studies were done towards the installation of TIMEPIX detectors in ATLAS in 2014-2015. For part of the analysis I used the Medipix frame work (MAFalda) implemented by John Idàrraga. The TIMEPIX results were presented in two conferences; IWORID 2013 and COMO 2013.

Apart from my project, I contributed to the ATLAS experiment with on-line and off-line shifts. I did ATLAS reconstruction class 2 shifts and participated in the data taking at the beginning of 2013 as a run control shifter (on line shifts).

INTRODUCTION

The Large Hadron Collider (LHC) is a high- energy particle accelerator with a circumference of 27 km designed to achieve a center- of- mass energy of 14 TeV and 1148 TeV for head- on collisions of protons and lead ions, respectively. Of the seven experiments installed around the trajectory of the LHC, ATLAS (A Toroidal LHC ApparatuS) is the largest experiment. The work presented in this study is based on data collected from the ATLAS-MPX (MPX) detectors installed within the ATLAS detector.

The beam energy and the luminosity are the most important performance parameters for the operation of particle colliders such as the LHC. The luminosity is a parameter that expresses the capability of a particle collider to produce a number of interactions or events. It is defined as the proportionality factor between the number of events generated per second and the cross section. Therefore, the more precise evaluation of the luminosity allows a better measurement of the cross section.

This thesis describes the calibration and performance of the MPX detectors (a network of 16 Medipix2 silicon based detectors) as luminosity sub-detectors of proton-proton collisions. The MPX detectors are primarily designed to perform measurements of the field composition (photons, neutrons and charged particles) and its spectral characteristics in the ATLAS cavern. The wide dynamic range of the MPX detectors and their high sensitivity to the beams movements and changes allows the measurement of the radiation background, the induced activity during and after the collision periods, and the luminosity summed over all colliding bunch pairs.

The luminosity calibration method used in the ATLAS detector is based on the vander Meer (vdM) scans. Determination of the absolute luminosity is based on beam-separation scans and the machine parameters [2]. The three vdM scan sessions performed in April, July, and November 2012 are analyzed in this thesis. The results of this analysis will contribute to the overall luminosity determination of the 8 TeV proton-proton (pp) collisions recorded by the MPX detectors in 2012.

The first chapter is a brief overview of the LHC with its main seven experiments. More specifically, it will describe the ATLAS detector with its major active inner com-

ponents. Chapter two describes the characteristics of semiconductors and their use in building pixelated detectors with the emphasis on silicon-based detectors. Chapter 3 will describe the characteristics of the Medipix2 detector and will give a brief overview of the MPX network in the ATLAS detector. The concept of luminosity is introduced in chapter 4, and a special part is dedicated to explain the theory of vdM scans used in the analysis. The analysis of the three calibration scans performed in 2012 are presented in chapter 5. This chapter is dedicated to illustrate the capability of the MPX detectors close to the vacuum chambers, such as MPX01, of providing relative- luminosity measurements during the three vdM calibration scans performed in 2012.

CHAPTER 1

THE ATLAS EXPERIMENT AT CERN

The purpose of this chapter is to give a brief overview of the ATLAS (A Toroidal LHC Apparatus) experiment performed at CERN and to introduce the use of the MPX detectors, which were installed in 2008 in the ATLAS cavern and have collected data independently of the ATLAS data-recording chain from 2010 to 2013. The MPX detectors were installed in order to study the radiation field in the ATLAS detector (including neutron fields) produced from proton-proton and ion-ion collisions at the LHC (Large Hadron Collider). Currently the LHC is being upgraded, and the network of the MPX detectors will be upgraded to include Timepix detectors which will exploit the time over threshold (TOT) mode of operation and will be also used to measure the time of flight (TOF), of particles produced in collisions compared to background particles.

1.1 ATLAS Experiment

The LHC collider is a high-energy particle accelerator with two circular vacuum chambers with a circumference of 27 km and located underground at a depth of 100 m. It was built by the European Organization for Nuclear Research (CERN) close to Geneva and lies beneath the Franco-Swiss border. Laid in the former LEP tunnel at CERN, the LHC has been designed to produce head-on proton-proton and lead ions collisions at a center-of-mass energy of 14 TeV and 1148 TeV, respectively. The LHC is in operation since Autumn 2008, and first collisions were recorded in Spring 2010 at beam energy of 3.5 TeV achieving a center-of-mass of 7 TeV. The beam energy was increased to 4 TeV achieving a center-of-mass energy of 8 TeV in 2012. Seven experiments have been installed along the trajectory of colliding protons and ion beams: ATLAS, CMS (Compact Muon Solenoid), LHCb (Large Hadron Collider beauty), ALICE (A Large Ion Collider Experiment), TOTEM (TOTAL Elastic and diffractive cross section Measurement), LHCf (Large Hadron Collider forward), and MoEDAL (Monopole and

Exotics Detector At the LHC). The ATLAS experiment is the main focus of our research.

The ATLAS experiment is designed to make use of the unprecedented energy available at the LHC in order to understand the phenomena which involve highly massive particles that cannot be observed with lower- energy accelerators, and to explore the physics beyond the Standard Model (SM) of particle physics. While the SM explains the interactions between subatomic particles governed by the strong and electroweak forces, it predicts the Higgs particle. The Higgs particle through the so-called Higgs mechanism is responsible for the dynamical generation of the mass of elementary particles by their interaction with the Higgs field that permeates all space. The announcement of the historical event of the discovery of the Higgs Boson on the 4th of July 2012, by the ATLAS and CMS collaborations at CERN is pivotal to the SM because it explains why some fundamental particles have mass when the symmetries controlling their interactions require them to be massless. The discovery was recognized by awarding Professor François Englert and Professor Peter Higgs [3] the Nobel prize for physics in 2013 for their pioneering works in identifying the electro-weak-symmetry-breaking mechanism . Once the LHC accelerator is back into operation in 2015, scientists can confirm if the discovered Higgs particle is the SM Higgs or not. They will also continue their research in fields beyond the SM such as Dark matter and supersymmetry, more generally.

1.2 The ATLAS Detector

The ATLAS detector is the largest volume particle detector ever constructed. It has a cylindrical structure of 45 m length, 25 m in diameter and weights about 7000 tons. It consists of a series of ever- larger concentric cylinders around the interaction point where the protons and ions beams of the LHC collide. It is composed of four major components; the Inner Detector, the Calorimeters, the Muon Spectrometer, and the magnet systems [4], as illustrated in figure 1.1.

The inner detector is designed to track charged particles through their interactions with the detector active materials at discrete points, showing detailed information about the types of particles and their momentum. It consists of three layers of silicon pixel de-

tor (Pixel), followed by four double layers of silicon strips known as the SCT (Semi Conductor Tracker). The outermost component of the inner detector is the TRT (Transition Radiation Tracker) that consists of layers of long tubes filled with Xenon and CO₂ gas.

The system of Calorimeters is found outside the solenoidal magnet that surrounds the inner detector. The calorimeters are the components that absorb and measure the energy deposited by particles passing through the detector. They can be divided into two major calorimeter systems: an inner electromagnetic calorimeter (EMC) including a barrel and an outer hadronic calorimeter (HAD). The EMC absorbs particles energy through electromagnetic interactions that embody photons and charged particles. The barrel EM calorimeter is distinct because of its accordion shaped lead electrodes arranged in a zig-zag radially from the beam and the use of Liquid argon (LAr) as sensitive medium. The new accordion geometry concept introduces fast readout and good hermiticity. The use of LAr as an active material helped solving the problem of the detector stability and radiation hardness, while giving excellent electromagnetic energy resolution [5].

The second major system: the hadron calorimeter measures the energy deposited by hadrons strongly interacting in their sensitive medium, after passing through the EMC. They are very efficient in jet identification, measurement of the jets direction and total missing transverse energy. The main part of the hadronic calorimeter is known as the Tile calorimeter (TileCal) with ion absorbers and scintillator tiles as sensitive medium and the far-forward section of the hadronic calorimeter is known as the forward calorimeter (FCal) which uses liquid argon as active material and tungsten and copper as absorbers.

The third component, the Muon Spectrometer is designed to measure the momentum of muons. It is a gigantic tracking system with a radius that extends from 4.5 m up to 11 m. This tremendous size is needed to precisely measure the momentum of muons showered through the former parts of the ATLAS detector before reaching the muon spectrometer. It is formed of three parts: i) three toroidal magnets, ii) a set of 1200 chambers that precisely measure the tracks of the outgoing muons, and iii) a set of triggering chambers with accurate time-resolution.

The magnet system is the last part of the ATLAS detector which consists of two large

superconducting magnet systems that allow the curving of the trajectories of the particles to give a precise measurement of their momentum. The inner solenoid produces a field of 2 T around the inner detector which is enough to allow even very energetic particles to curve so that their momentum can be determined. The outer toroidal located outside the calorimeters and within the muon system generates a non uniform magnetic field that varies between 2 T up to 8 T.

At the ends of the detector, there are three small detectors: LUCID, ALFA, and ZDC. LUCID (LUminosity measurement using Cerenkov Integrating Detector) and ALFA (Absolute Luminosity For ATLAS) that are dedicated to measurement of the luminosity produced by collisions, while ZDC (Zero-Degree Calorimeter) measures the centrality of heavy ions collisions [4].

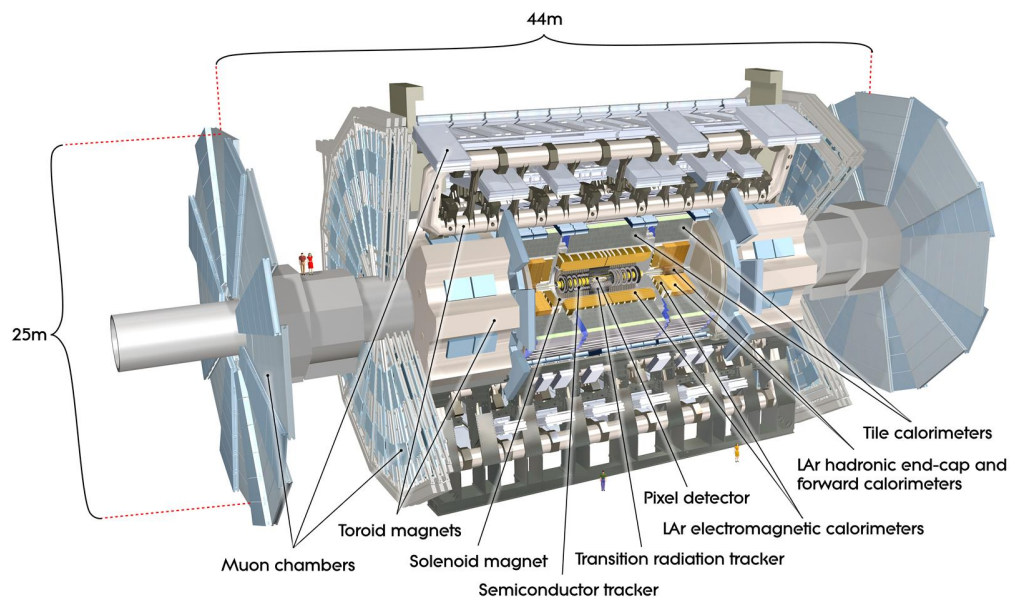


Figure 1.1: A computer generated view of a vertical section of the ATLAS detector illustrating its active components [3]

CHAPTER 2

SEMICONDUCTORS AND INTERACTIONS OF PARTICLES WITH MATTER

The purpose of this chapter is to briefly review the fundamental characteristics of semiconductors and their applications in pixelated detectors. Semiconductors are widely used in detectors. Their material has an electrical conductivity that lies between that of a metal and that of an insulator. Semiconductors possess the property of changing their conductivity and modulating their electrical properties by the addition of impurities (doping), or by interacting with an applied electric field or light. This makes semiconductors very useful in building detectors and devices that can convert an energy input. The most commonly used materials for semiconductors are silicon (Si), germanium (Ge), gallium arsenide (GaAs), and cadmium telluride (CdTe).

2.1 Fundamentals of semiconductors

The comprehension of semiconductors requires an understanding of solid materials, crystals, used to form them. In this thesis, we are using silicon semiconductors. Silicon crystals consist of atoms that are ordered in a diamond lattice where each atom has a covalent bond with four adjacent atoms forming a tetrahedron. Crystals have two specific properties that are essential to evaluate the current in a semiconductor: the amount of fixed and mobile charges present in the material, and the movement of the charge carriers through the semiconductor.

The main characteristic of semiconductors is the presence of a band gap (referred to as an energy gap). Energy bands in crystalline materials are a collection of a large number of closely spaced energy levels. More specifically, it is the sum of the individual energy levels of electrons surrounding each atom. Pauli Exclusion Principle does not allow electrons to have the same energy levels which results in a set of closely spaced energy levels known as an energy band. Energy bands differ among various materials as shown in Figure 2.1a.

The band gap is the energy difference (E_g) between the valence band (VB) and the conduction band (CB). The characteristics of the energy-band structure are responsible for the electrical properties of different materials. In semiconductors, electrons are restricted to a number of energy bands and forbidden from others. However, electrons (e) are able to jump from a valence band to a conduction band leaving behind holes (h), if the excited electrons have a minimum energy larger than the energy of the gap. Electrons can gain this energy either by absorbing a photon (light). There is a high probability to create a pair of electron-hole by optical absorption.

Undoped semiconductors at $T = 0$, have an empty CB and a full VB. The concept of holes is used to refer to the missing electrons in the almost filled VB. Holes behave in the same way as electrons when occupying the same energy states but they carry a positive charge. Therefore, electrons act as negative charge carriers and holes act as positive charge carriers. In undoped semiconductors the charge carriers are known as intrinsic charge carriers and the concentration of the intrinsic charge carriers is principally governed by the factor ($e^{E_g/2k_B T}$), where k_B is Boltzmann constant and T is the temperature in kelvin.

Semiconductors can have two types of transitions: direct and indirect. Direct transition occurs when the crystal absorbs a photon creating an electron-hole pair. While in the indirect transition, the absorbed photon is combined with the absorption of a phonon as the extrema of the valence band and conduction band are not aligned as shown in Figure 2.1b. The relationship between the concentration of charge carriers and the conductivity will be explained further in this chapter.

2.2 Electrical conductivity; mobility

It is possible to create an electrical current in semiconductors by applying an external potential which will generate an electrical field causing the charge carriers to drift with a velocity v . The electrons will move towards the anode while the holes will move towards the cathode, contributing to an electrical current. The mobility of the charge carriers is proportional to their velocity and inversely proportional to the electrical field,

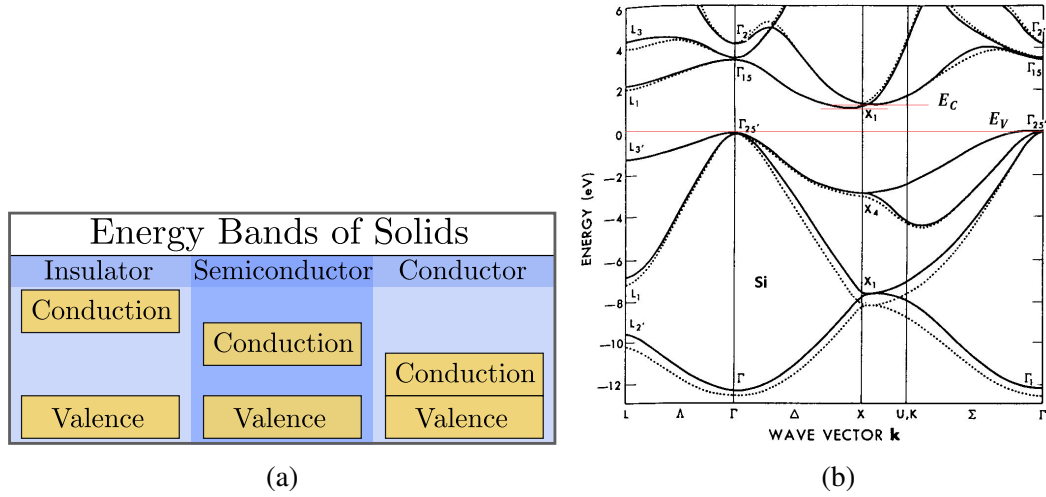


Figure 2.1: (a) Energy band in different solids; insulator, semiconductor, and conductor. (b) Structure of the energy band in Silicon. The indirect transition in silicon is clearly visible as the minimum of the CB is not aligned with the VB [6].

$$\mu_{e,h} = |v|/E. \quad (2.1)$$

The velocity of a charge q is

$$v = \frac{q\tau E}{m}, \quad (2.2)$$

Then, the mobility can be expressed as

$$\mu_{e,h} = \frac{|q|\tau_{e,h}}{m_{e,h}}, \quad (2.3)$$

where τ_h is the collision time of holes, τ_e is the collision time of electrons, m_e is the mass of electrons charge carriers, m_h is the mass of holes charge carriers, q is the electronic charge, and E is the electric field. For example, the mobility of electrons in silicon at 300 K is $1350 \text{ cm}^2\text{V}^{-1}\text{s}^{-1}$ and $480 \text{ cm}^2\text{V}^{-1}\text{s}^{-1}$ for holes [6].

The conductivity σ of a semiconductor is expressed as:

$$\sigma = nq\mu_e + pq\mu_h, \quad (2.4)$$

where n and p are the charge carriers concentration, electrons and holes, respectively. There are two other important quantities: the resistivity ρ which is the inverse of the conductivity, and the electrical current density J which is represented as [7]:

$$J = \sigma E. \quad (2.5)$$

2.3 p-n Junction

Intrinsic semiconductors are the ones that have the same density of electrons and holes ($n = p$). However, it is possible to dope a semiconductor by adding impurities to pure crystals. As described earlier, silicon is a tetravalent crystal that can perform four covalent bonds with neighboring atoms. Therefore, this allows adding either pentavalent impurities such as phosphorus or arsenic having extra electrons producing a semiconductor of n - type or trivalent impurities such as boron having extra holes producing semiconductors of p - type.

Doped materials of n - type are called donors, while doped materials of p - type are called acceptors. The concentration in terms of the charge carriers is: [8]

$$np = 4 \left(\frac{k_B T}{2\pi\hbar} \right)^3 (m_e m_h)^{3/2} \exp\left(\frac{-E_g}{k_B T}\right). \quad (2.6)$$

2.4 depletion zone

A fundamental unit of semiconductor devices is formed when an n -type semiconductor is joined to a p -type semiconductor creating a $p - n$ junction. A junction diode is a device based on a single $p - n$ junction, and the role of the diode is to pass current in one direction (one- way valve for current). Some of the free electrons in the n -region (mobile n -side donor electrons) diffuse across the junction and combine with holes forming negative ions. However, they leave behind them immobile positive ions at the donor impurity side.

Figure 2.2 shows that p -type region has more holes coming from the acceptor impurities and the n -type region has extra electrons. When a $p - n$ junction is created, some

of the electrons that have reached the conduction band in the n -region are free to diffuse across the junction and to combine with holes. Filling a hole makes a negative ion that leaves behind it a positive ion on the n -side. A space charge builds up, creating a depletion region ($x_d = x_p + x_n$ in Figure 2.2) that inhibits any further electron transfer unless it is helped by putting a bias on the junction [9].

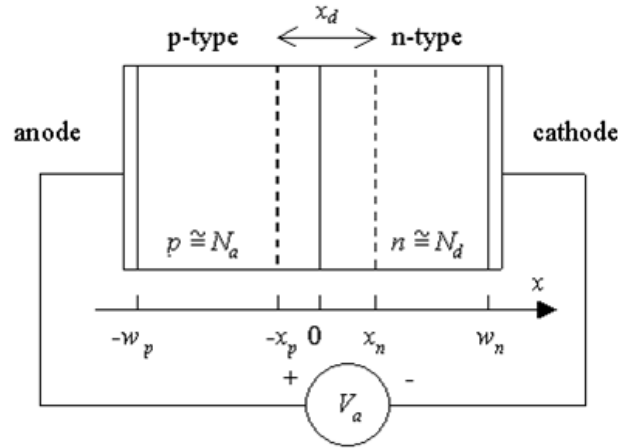


Figure 2.2: Depletion zone [10].

The width w of the depleted zone depends on the concentration of donors N_D and acceptors N_A

$$w = x_n + x_p = \sqrt{\frac{2\varepsilon V_o}{q} \frac{N_A + N_D}{N_A N_D}}, \quad (2.7)$$

where ε is the dielectric constant of the medium ($\varepsilon = 1.05 pF/cm$ in silicon), and V_o is the electrical contact potential of about 0.6 V for silicon based detectors [8]. Applying an external potential V_e enlarges the width of the depletion zone which becomes equal to

$$w = \sqrt{\frac{2\varepsilon(V_o + V_e)}{q} \frac{N_A + N_D}{N_A N_D}}. \quad (2.8)$$

The width of the depletion zone is approximated as

$$w \simeq \sqrt{\frac{2\varepsilon(V_o + V_e)}{q N_{eff}}}, \quad (2.9)$$

where $N_{eff} = |N_A - N_D|$ is the effective concentration.

2.5 Passage of Particles Through Matter

The basic principle behind any particle detector uses the fact that particles which traverse matter may create free charge carriers via ionisation which can be extracted and collected by using an electric field. The electric signal can then be processed by read-out electronics and allows one to measure the energy deposition and - in a next step - to infer the energy of the particle itself. Particles and photons interact with matter, where they deposit their energy via electromagnetic or nuclear process.

Heavy charged particles (p, α . . .) passing through matter interact with electrons and nuclei in the matter. These interactions are due to collisions which lead to excitation or ionization. Excitation is raising the energy of the orbital electrons into higher states in the atom, and ionization is the production of ion-electron pairs.

For an incoming particle with a rest mass m_p , velocity $v = \beta c$ (where c is the speed of light), and a charge number z ¹, the energy-loss formula known as Bethe-Bloch Formula is

$$-\frac{dE}{dx} = \frac{2\pi n z^2 e^4}{m v^2} \left\{ \ln \left[\frac{2 m v^2 W_m}{I^2 (1 - \beta^2)} \right] - 2\beta^2 - \delta - U \right\}, \quad (2.10)$$

where m is the rest mass of the electron, n is the number of electrons per cm^3 of the traversed material, I is the mean excitation energy of the atoms of the material, W_m is the maximum transferable energy from the incident particle to atomic electrons, δ is the correction for the density-effect, and U is the term related to the non participation of electrons of inner shells [11].

When the kinetic energy of particles is at least twice as large as their rest mass, (electrons greater than 1 MeV, and protons greater than 2 GeV), they can be considered as Minimum Ionizing Particles (MIP). Since the ionization loss of these particles are only weakly dependent on their momentum, it is generally accepted that minimum ionizing

1. z is the coefficient that, when multiplied by the elementary charge, gives the ion's charge [Wikipedia 2013]

particles produce an even distribution of free charge carriers along their paths.

Photons (electrically neutral particles) are undergoing interactions leading to partial or total transfer of the photon energy to electrons. In the case of photon absorption, the most effective processes are photoelectric (PE), Compton scattering (C), and pair production (PP) of electrons and positrons.

The linear attenuation coefficient μ describes the rate of energy loss by a photon per centimetre within a medium of density ρ (g/cm³). It has units of cm⁻¹, and is presented as:

$$I(x) = I_o e^{-\mu x}, \quad (2.11)$$

where $I(x)$ is the intensity at depth of x cm, I_o is the original intensity, and μ is the linear attenuation coefficient represented as

$$\mu = (N_A \rho / A) \sigma, \quad (2.12)$$

where σ is the total cross section $\sigma = \sigma_{PE} + \sigma_C + \sigma_{PP}$, (σ_{PE} , σ_C , σ_{PP} are the photoelectric, Compton scattering, and pair production cross-sections, respectively); N_A is Avogadro number, A is the atomic mass, and ρ is the density in (g/cm³).

The mass attenuation coefficient μ/ρ (cm²g⁻¹) describes the rate of energy loss by a photon as it traverses a medium of density ρ . Then, the attenuation equation becomes:

$$I(x) = I_o e^{-\frac{\mu}{\rho} \cdot \rho x}. \quad (2.13)$$

Neutrons are classified depending on their energies; fast neutrons have an energy larger than 1 MeV, thermal neutrons have an energy of 25 meV. Fast neutrons can interact in the silicon sensor via the reactions: Si(n,p)Al and Si(n, α)Mg with threshold of 4 and 2.7 MeV, respectively. In practice silicon-based detectors are coated with neutron converter layers (see section 3.5) in order to increase their sensitivity to neutron fields.

CHAPTER 3

THE MEDIPIX2 (MPX) DETECTOR IN ATLAS

The Medipix project [12] is a collaboration between several universities and research institutes worldwide coordinated by the CERN microelectronics group with the goal to design and develop a family of pixelated detectors which became the Medipix detectors family. This chapter describes the characteristics of the Medipix2 (MPX) detector which has been used for the research presented in this thesis.

3.1 Description of the MPX detector

Detectors at the LHC are constantly upgraded to better detect all types of incoming particles. New detectors are required for monitoring the tracks of primary and secondary particles produced by colliding beams. Detectors are dedicated to resolve different types of tracks left by various interacting particles and to assign them to primary or secondary vertices. For this reason, several types of position sensitive detectors have been developed.

Detectors of the Medipix family are photon counting pixel detectors. They descend from silicon pixel detectors which are used in various research fields and applications such as particle and nuclear physics, as well as medical and industrial imaging.

The MPX detector is a hybrid detector composed of two layers. The upper layer is the active one usually a $p^+ - n - n^+$ junction of $300 \mu\text{m}$ thick silicon sensor bonded onto a layer of electronics used for the read-out¹. The electronics are bump-bonded to the cathode as shown in Figure 3.1a Label (B). They are responsible to collect the produced charge from the interactions of the incident particles with the sensor, to be then processed by a CMOS (Complementary Metal- Oxide- Semiconductor) electronics layer. This allows one to have an active area of 256×256 pixels, each squared pixel has a size of $55 \mu\text{m}$, Then, the MPX detector has a total area $14.08 \text{ mm} \times 14.08 \text{ mm}$.

1. The semiconductor sensor layer can be also GaAs (Gallium Arsenide), or CdTe (Cadmium Telluride) in which the interacting incident radiation produces an electron/ hole column.

Figure 3.1b shows a MPX detector with a USB (Universal Serial Bus) readout; label (A) is the sensor layer where the actual interaction with the incident particle occurs. Label (C) refers to the chipboard with the electronics that is needed for the power supply of the ASIC (Application- Specific Integrated Circuit) as well as the data transfer from and to the readout label (D), which extracts the data from the detector. The semiconductor layer is connected via bump bonds to the pixelated electrical part, the ASIC [13] as seen in figure 3.1a.

Figure 3.2 shows the MPX chipboard with dimensions of 47 x 79 mm². The MPX chip is located in the middle upper side of the board, and in the upper left corner is the LEMO² connector for detector bias voltage. The chipboard is connected via 68-pin VHDCI8 connector to the read-out electronics. The layout of the MPX chip is shown in Figure 3.3. The layout is designed to minimize the dead area between chips covering large areas when putting several chips together as detailed in [14].

Each square pixel of the MPX detector consists of 504 transistors. It can be divided into an analog and a digital part as shown in Figure 3.4. Both the analog and digital circuitry has been designed to operate with independent 2.2 V power supplies. The total power consumption is about 500 mW. The analog part consists of a charge preamplifier with DC leakage current compensation, a test capacitance, and two branches of identical discriminators. The octagonal bump bond opening used for connection with sensor is placed on top of the analog side and has a diameter of 20 μm [14].

The detector is connected to a computer using a USB interface, and it is controlled using a special software known as Pixelman [15]. Pixelman is used to record the data and to set and modify the operational parameters of the detector.

An incident particle creates electron-hole pairs that are drifting under the effect of an electrical field. The charges are collected by the cathode and the signal is amplified. The signal is compared to a certain threshold³; if the signal is above threshold the counter is

2. **LEMO** is both the name of an electronic and fiber optic connector manufacturer. The company took its name from the company founder, engineer **Léon Mouttet**.(Wikipedia 2013)

3. The minimum kinetic energy that a pair of traveling particles must have when they collide is known as the threshold energy. The MPX detector can operate at low threshold and at high threshold typically of 10 keV and 230 keV, respectively.

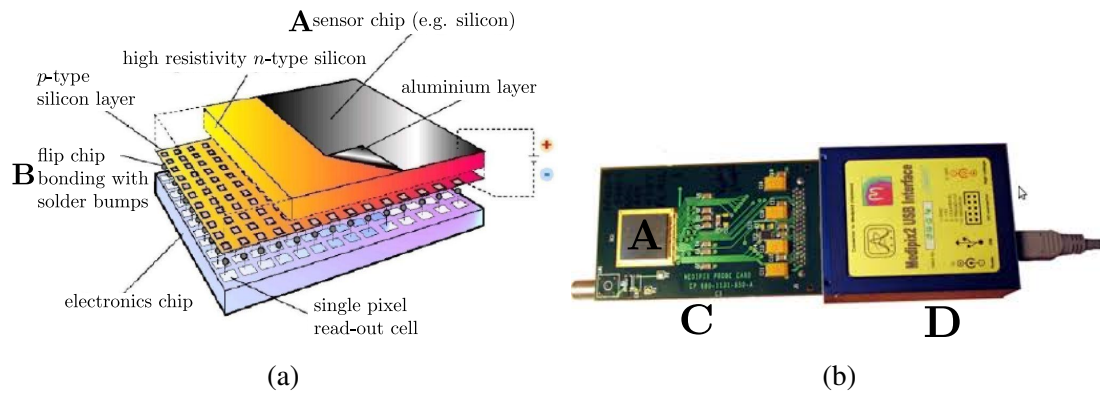


Figure 3.1: Picture of a scheme of the bump bonded sensor layer (a), and a picture of a MPX detector with a USB-readout (b). Label (A) indicates the sensor layer; (B) the bump bonds with the pixelated ASIC; (C) the chipboard that contains the electronics and (D) the USB-readout [13]

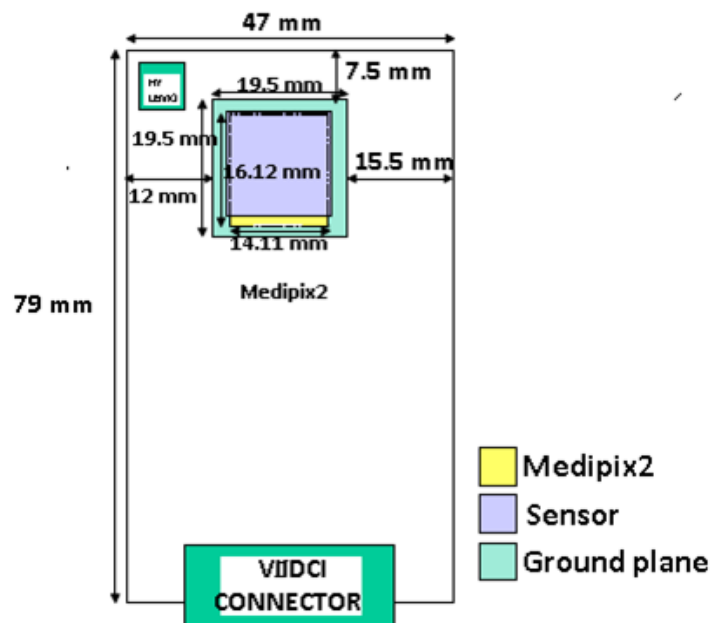


Figure 3.2: MPX (Medipix2 in the figure) chipboard [14]

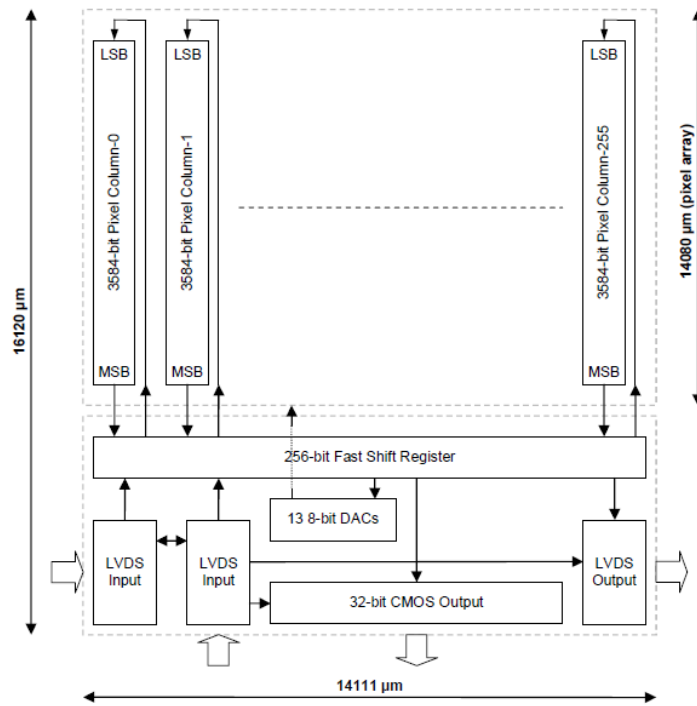


Figure 3.3: MPX surface plan and block diagram [14]

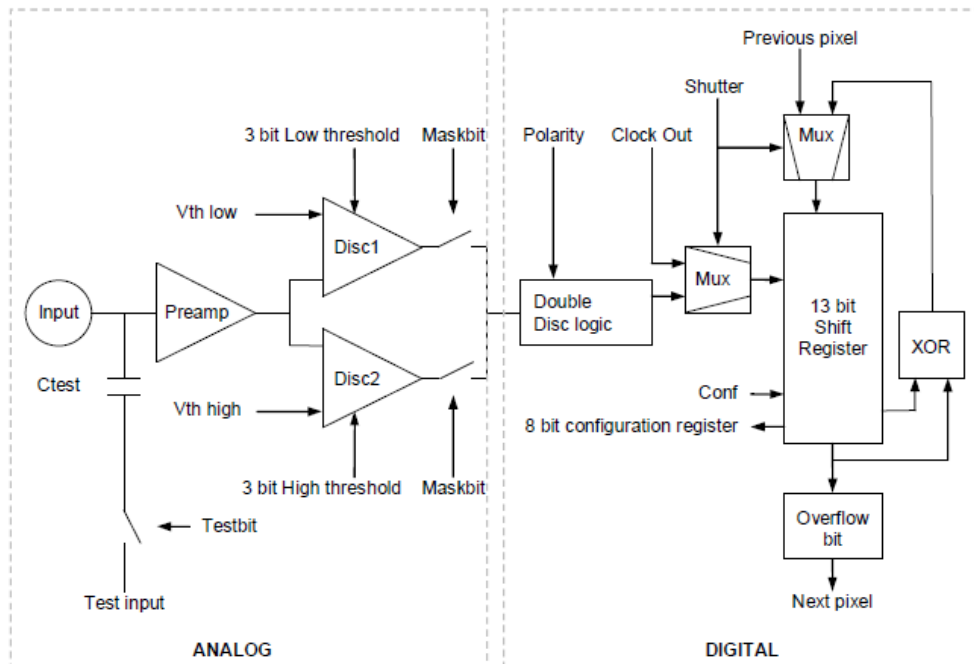


Figure 3.4: MPX pixel cell block diagram [14]

incremented by 1, if not it counts 0. For a certain exposure time, an incident particle will activate one or several pixels forming a cluster of adjacent pixels, known as an event. The number of events in each pixel is counted by the electronics and distinguished by discriminators that record events within a selected energy range. The acquired readout of the counters of all pixels yields an image called a frame that represents the recorded status of all pixels per exposure time. Figure 3.5 illustrates the radiation field in ATLAS recorded on the 29th of September 2011 with MPX01.

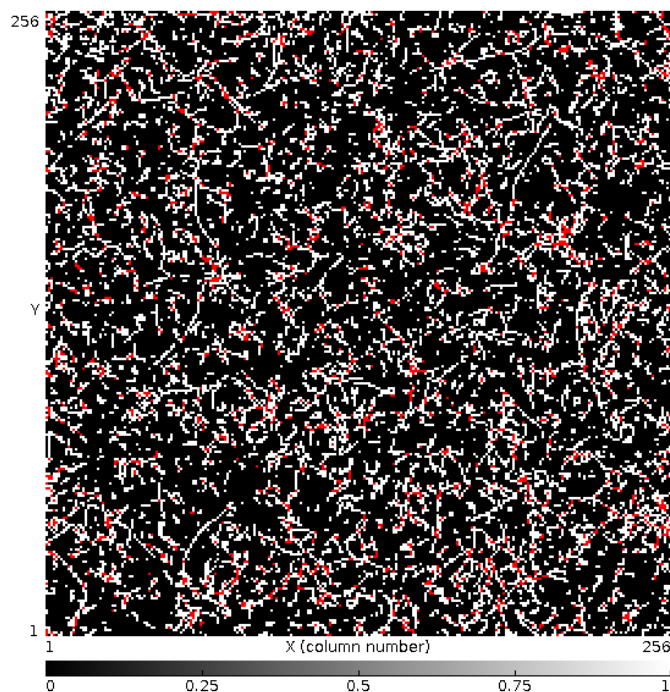


Figure 3.5: Radiation field in ATLAS as seen on the 29th September 2011 by MPX01 placed perpendicular to the beam axis facing the ATLAS Interaction Point (IP1) with an exposure time of 30 s during a van der Meer Scan (vdM) at low threshold (LT). Note that red dots represent noisy pixels (see section 5.2 for more details) [16].

The lateral spread of the charge carriers from the interaction of an ionizing particle in the silicon layer of the detector causes a sharing of the charge among adjacent pixels leaving different shapes of formed clusters [17]. Different particles leave different tracks that are distinguishable once a pattern recognition is established as explained in section 3.3.

3.2 Characterization of tracks with MPX detectors

A software for pattern recognition of tracks uses the cluster shape left in the detector to identify the type of incident particles. Figure 3.6 shows different examples of pixel shapes generated by different types of particles.







Dots		Photons and electrons
Small blobs		Photons and electrons
Heavy blobs		Heavy ionizing particles
Heavy tracks		Heavy ionizing particles → Incidence is not perpendicular to the detector's surface (Bragg curve)
Straight tracks		MIP
Curly tracks		Energetic electrons

Figure 3.6: Different pixel shapes generated by various types of particles [17].

Measured particles are classified in four main categories: (i) Minimum Ionizing Particles (MIPs): muons and high energy protons registered as straight tracks on the whole sensor. (ii) Low Energy Transfer Particles (LETP): electrons and photons registered as dots, small blobs and curly tracks on the whole sensor, including other high energy particles which can be recognized also as small blobs. (iii) High Energy Transfer Particles (HETP): low energy protons (with high ionizing power, roughly below 80 MeV) and ions, fast neutrons effectively detected via recoiled protons or carbon ions from the polyethylene converter, energetic hadrons (including fast neutrons) interacting strongly in the silicon sensor, which are registered as heavy blobs and heavy tracks on the whole sensor except the ${}^6\text{LiF}$ region. (iiii) Thermal neutrons: neutrons with energy of 25 meV detected via interactions in enriched ${}^6\text{LiF}$ converter registered as heavy blobs in the ${}^6\text{LiF}$ region [18].

3.3 The MPX network

The MPX detectors are designed for the detection of different types of radiations. These detectors were installed in the ATLAS experiment at 16 positions as depicted on

figure 3.7 and figure 3.8 where the exact coordinates of their locations since 2008 are summarized in table 3.I and have been successfully operated since then.

The MPX detectors collect data independently of the ATLAS data- recording chain. Designed primarily to provide information on the radiation composition within the ATLAS detector, the MPX detector also measures the background radiation in both the experimental hall and its surroundings, and the induced radioactivity in the ATLAS environment after collisions. The MPX setup has been used to measure the luminosity of proton- proton and lead- lead collisions as discussed in details in chapter five.

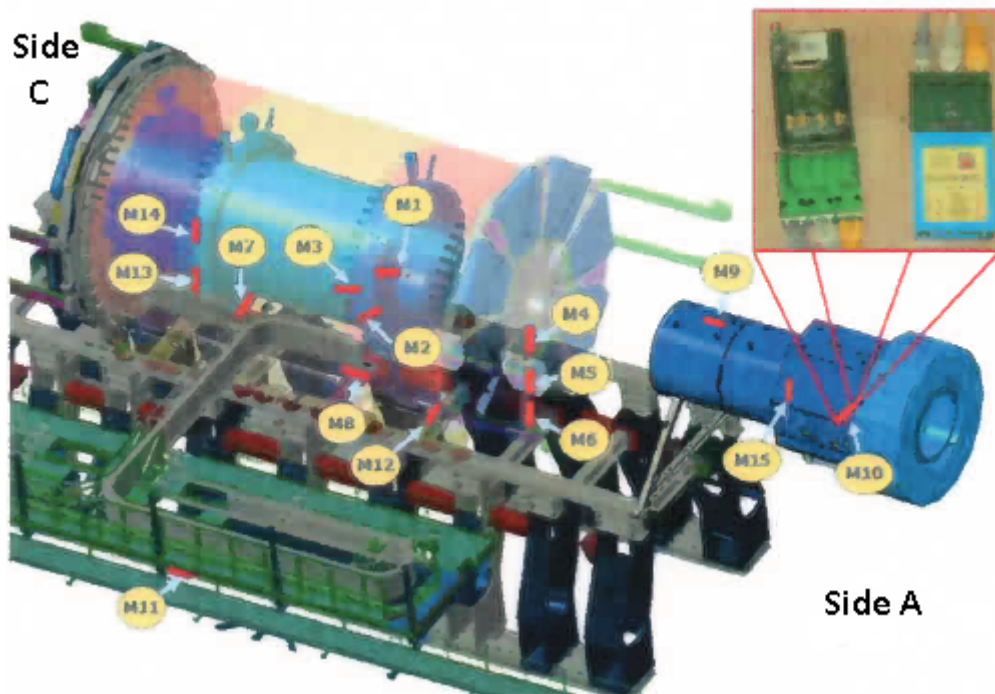


Figure 3.7: The network of MPX detectors in ATLAS [16]. The precise MPX detectors coordinates of their locations are given in table 3.I. Note that there are some detectors on 'Side A' and others on 'Side C' of the ATLAS detector.

3.4 Modes of operations and pattern track recognition

The lowest threshold (LT) typically 10 keV is set at a level to allow the MPX detectors to reduce the overlap among tracks in frames. The operation of MPX detectors at

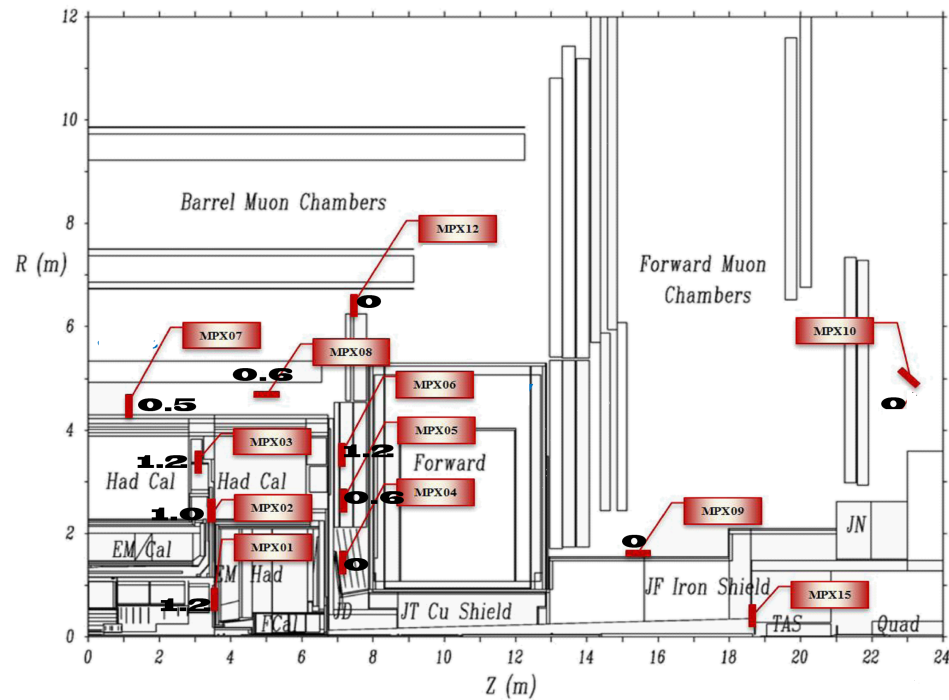


Figure 3.8: Locations and orientations of MPX detectors with their labels for 12 of the 16 MPX detectors on side A in ATLAS. MPX13 and MPX14 are placed on side C (see Figure 3.7) almost symmetrically to MPX01 and MPX02. MPX11 is out of R-axis range (see Table 3.I) and MPX16 is located in USA15. The detectors are oriented in three different directions: Perpendicular to the beam axis (Z-axis) facing the IP1: MPX01, MPX02, MPX03, MPX04, MPX05, MPX06, MPX07, MPX12, MPX13, MPX14, MPX15; parallel to the beam axis: MPX08, MPX09, MPX11, MPX16; at 45° to the beam axis: MPX10 [18].

Table 3.I: MPX detectors location and position with respect to the ATLAS interaction point IP1. X axis points to the center of the LHC, Y axis points in the vertical plane, Z is along the beam axis, and $R = (X^2 + Y^2)^{1/2}$ is the distance from the beam axis at position Z . The detectors were in operation during the all beam-on and beam-off LHC periods [18].

Device	Location description	X [m]	Y [m]	Z [m]	R [m]
MPX01	between ID and JM plug	-0.71	0.29	3.42	0.77
MPX02	between TILE and EB	-2.23	-1.12	3.42	2.50
MPX03	between TILE and EB	-3.45	0.93	2.94	3.57
MPX04	on the Small Wheel	-0.65	-1.30	7.12	1.30
MPX05	on the Small Wheel	-0.55	-2.36	7.20	2.36
MPX06	on the Small Wheel	-0.65	-3.36	7.20	3.36
MPX07	top of TILECAL barrel	-4.53	0.79	0.35	4.59
MPX08	top of TILECAL EB	-4.37	-0.53	4.02	4.40
MPX09	on the JF cylinder	0.00	1.56	15.39	1.56
MPX10	cavern wall HO	-3.96	3.36	22.88	5.19
MPX11	cavern wall USA side	-16.69	0.05	4.86	16.69
MPX12	on the EIL 4	-6.25	0.00	7.23	6.25
MPX13	between TILE and EB, C	-2.21	-1.02	-3.42	2.44
MPX14	between ID and JM plug, C	-0.71	-0.30	-3.43	0.77
MPX15	at the back of LUCID	0.19	-0.08	18.74	0.20
MPX16	USA15	-39.48	0.90	-6.55	39.48

high threshold (HT), typically 230 keV, allows the discrimination of particles with low energy transfer (LETP). The resulting frames from both cases could be analyzed using two different modes: the cluster- tracking mode and the pixel- hits counting mode.

The preferred MPX mode of operation, the cluster- tracking mode (tracking mode) is based on the analysis of the clusters formed from the interaction of particles in the sensor. The MPX detector is operated at a short enough exposure time to avoid the problem of tracks overlapping, allowing their better recognition. This mode of operation permits differentiation of clusters of adjoining activated pixels. The shape and size of the clusters is determined by the nature of the incident particle as it interacts with the silicon layer of the detector, the particle energy, and the particle incidence angle. The pattern recognition software Pixelman [15] is employed in the analysis of these clusters. Figure 3.9 illustrates various tracks left by different particles: LETP particles such as low energy X-rays and electrons will leave a dot (label 1) in figure 3.9), more energetic X-rays, electrons, and gamma rays leave small blobs (label 2) in figure 3.9) and curly tracks (label 3) in figure 3.9). While minimum ionizing particles (MIPs) such as muons leave long straight tracks (label 6) in figure 3.9). Heavy charged non- relativistic particles like low- energy protons and alpha particles leave two types of tracks depending on their angle of incidence and their energy; heavy blobs (label 4) in figure 3.9) for small angles of incidence; or heavy tracks (label 5) in figure 3.9) for larger angles of incidence [18].

The second mode of operation is the pixel- hits counting mode (counting mode) that analyzes the frames by summing all the registered hits in all clusters. This mode is essential for the study of particle fluxes in high radiation environments. As the increase in the cluster rate in the end of 2011 has caused an increase in the overlap among clusters (overcomplicating the pattern recognition analysis) the counting mode was left as the only option in the analysis.

3.5 Neutron detection using the MPX detectors

One of the aims of the ATLAS- MPX collaboration is to study the neutron fluxes and therefore, the 300 μm silicon sensor in each MPX detector is covered with a mosaic of

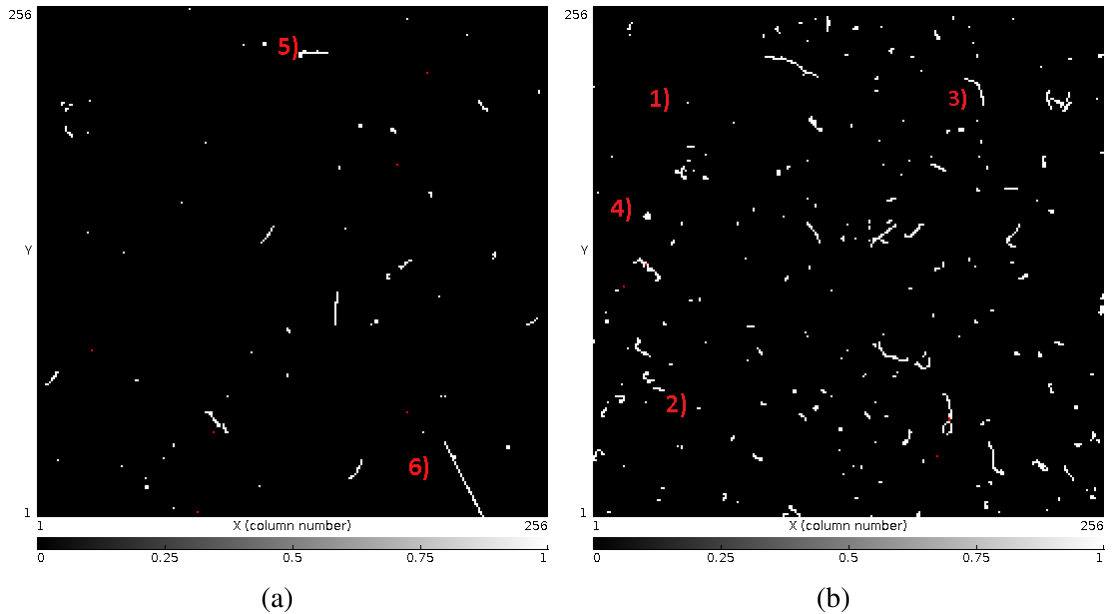


Figure 3.9: Background measurement in the ATLAS cavern in 2008 before any collisions period with a) MPX01, and b) MPX11. The inserted labels 1 to 6 describe the assignment of clusters to individual interacting quanta of radiation by means of the pattern recognition software as explained in the text [16].

converter layers. The interaction of incoming neutrons with these converter layers produce heavy charged particles, which are then detected in silicon. The neutron converter layers are shown in figure 3.10. They are divided into various regions to detect different types of neutrons (thermal and fast).

For the detection of thermal neutrons (25 meV energy), ${}^6\text{LiF}$ is used because it interacts with thermal neutrons via the reaction: ${}^6\text{LiF} + n \rightarrow \alpha + {}^3\text{H}$ with a cross section of 950 barns. The produced α -particles and tritons are detected in silicon (region (1) in Figure 3.10). The Fast neutrons with an energy ≥ 1 MeV are detected in the hydrogen-rich PE (Polyethylene) region. PE (region (2) in Figure 3.10) allows the use of recoil protons technique; it permits elastic collisions between neutrons and light hydrogen atoms: ${}^1\text{H}(n,n)p$. The recoiling protons are then detected in the underlying silicon layer. Aluminum layers are used to block background photons and electrons and to act as a kinematic threshold for the charged recoils [18].

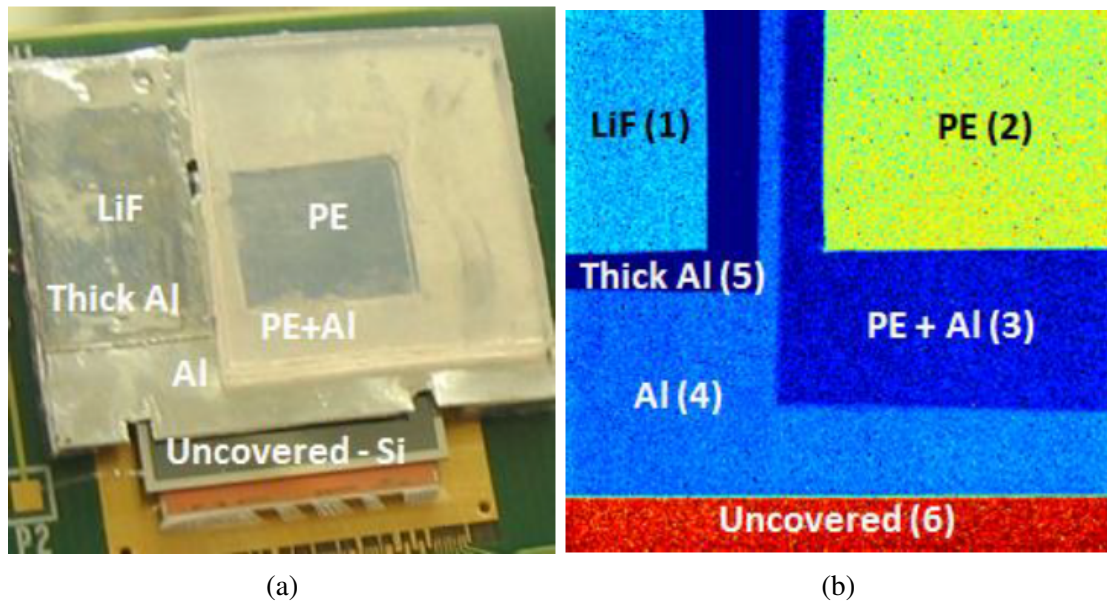


Figure 3.10: (a) The MPX sensor covered with neutron converter Layers: 1) LiF (5 mg/cm^2), 2) Polyethylene (PE) 1.3 mm thick, 3) PE (1.3 mm) layer above aluminum ($100 \mu\text{m}$), 4) Aluminum ($100 \mu\text{m}$), 5) Aluminum ($150 \mu\text{m}$), and 6) Uncovered silicon that is exposed to all incoming radiation where fast neutrons can be detected via the reactions: $\text{Si}(n,p)\text{Al}$ and $\text{Si}(n,\alpha)\text{Mg}$ with threshold of 4 and 2.7 MeV, respectively. (b) X-ray radiogram of the MPX detector conversion layers [18].

CHAPTER 4

CONCEPT OF LUMINOSITY

The aim of this chapter is to present the concept of luminosity and to derive the expressions of the absolute luminosity extracted from the machine and beam parameters used for the ATLAS detector measurements.

4.1 Concept of Luminosity

The luminosity ($\text{cm}^{-2}\text{s}^{-1}$) can be expressed as a function of the number of charges per beam and the convolved beams sizes at the point of interaction. It is used to quantify the performance of a particle collider. Precise measurements of the luminosity give an evaluation of the number of events generated by collisions, of the background levels and hence a better sensitivity to the signals. Uncertainties in the measurements of the delivered luminosity are the dominant source of systematic uncertainties in cross-section measurements. Therefore, accurate measurement of the luminosity of the colliding beams could have a significant contribution to the investigation of the SM and to new research in physics beyond the SM of particle physics [19].

The luminosity [\mathcal{L}] is represented as the proportionality factor between the number of events generated per second [dR/dt] and the cross section [σ] as:

$$\frac{dR}{dt} = \mathcal{L} \cdot \sigma. \quad (4.1)$$

The case of two colliding beams having different beam density distribution functions and different number of particles per bunch¹; as illustrated in Figure 4.1. The above equation could be generalized using a 3-D beam overlap function for \mathcal{L} as shown in Eq. 4.2. The overlap integral depends on the longitudinal position of the beams bunches and on the time they take to move towards each other. The distance of two bunches to the

1. Beams at the LHC are actually a collection of proton bunches. Each bunch is about 20-30 μm in diameter, and a few centimeters long [20].

center of the interaction region is $s_o = c \cdot t$ (see Figure 4.1, where s refer to the direction of the moving beams).

Then, one can write the luminosity as proportional to the overlap integral as:

$$\mathcal{L} = K \cdot \iiint_{-\infty}^{+\infty} \rho_1(x, y, s, -s_o) \rho_2(x, y, s, s_o) dx dy ds ds_o, \quad (4.2)$$

where $\rho_1(x, y, s, -s_o)$ and $\rho_2(x, y, s, s_o)$ are the time dependent beam density functions (see figure 4.1) and K is a kinematic factor needed because the two beams are moving against each other [21]:

$$K = \sqrt{(\vec{v}_1 - \vec{v}_2)^2 - (\vec{v}_1 \times \vec{v}_2)^2 / c^2}. \quad (4.3)$$

It is assumed that the beams meet at $s_o = 0$, head-on collisions ($\vec{v}_1 = -\vec{v}_2$), and all densities are uncorrelated in x and y planes. Therefore, one can factorize the beams density distributions and the luminosity becomes:

$$\mathcal{L} = 2N_1 N_2 f_r N_b \iiint_{-\infty}^{+\infty} \rho_{1x}(x) \rho_{1y}(y) \rho_{1s}(s - s_o) \rho_{2x}(x) \rho_{2y}(y) \rho_{2s}(s + s_o) dx dy ds ds_o, \quad (4.4)$$

where N_1 and N_2 are the intensities of the two colliding bunches, f_r is the revolution frequency and N_b is the number of colliding bunches pairs. An analytical calculation of the above integral is not always possible and a numerical integration may be re-

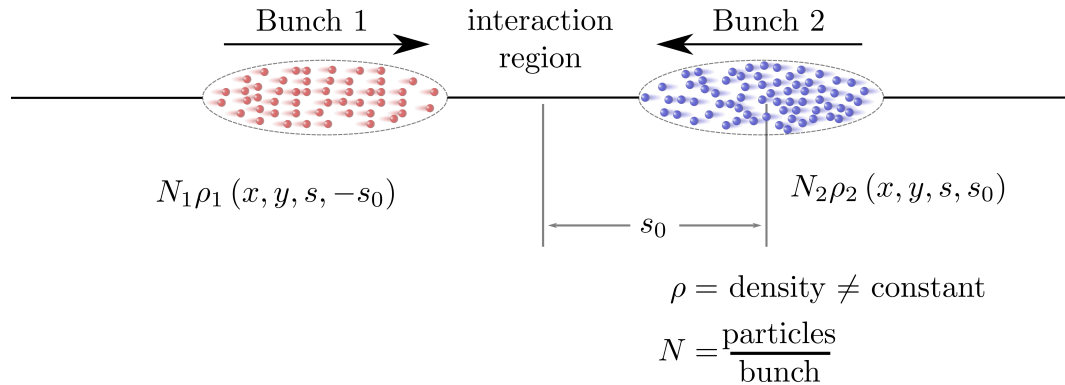


Figure 4.1: Schematic view of a colliding beam interaction.

quired. In many situations the beams follow "reasonable" profiles and solutions can be obtained [22].

4.2 Luminosity of colliding Gaussian beams

Usually one assumes Gaussian distributions of beam densities (profiles) of the following form:

$$\rho_{iz}(z) = \frac{1}{\sigma_z \sqrt{2\pi}} \exp\left(-\frac{z^2}{2\sigma_z^2}\right) \text{ where } i = 1, 2, z = x, y, \quad (4.5)$$

$$\rho_s(s \pm s_o) = \frac{1}{\sigma_s \sqrt{2\pi}} \exp\left(-\frac{(s \pm s_o)^2}{2\sigma_s^2}\right). \quad (4.6)$$

Assuming equal beams, i.e., $\sigma_{1x} = \sigma_{2x}$, $\sigma_{1y} = \sigma_{2y}$, $\sigma_{1s} = \sigma_{2s}$. In the situation of exactly head-on collisions of bunches travelling very close to the speed of light, the kinematic factor defined in equation 4.3 becomes 2.

Applying these assumptions and using the above Gaussian profiles in equation 4.4, the luminosity becomes:

$$\mathcal{L} = \frac{2 \cdot N_1 N_2 f N_b}{(\sqrt{2\pi})^6 \sigma_s^2 \sigma_x^2 \sigma_y^2} \iiint \int e^{-\frac{x^2}{\sigma_x^2}} e^{-\frac{y^2}{\sigma_y^2}} e^{-\frac{s^2}{\sigma_s^2}} e^{-\frac{s_o^2}{\sigma_s^2}} dx dy ds ds_o. \quad (4.7)$$

Using the formula $\int_{-\infty}^{+\infty} e^{-at^2} dt = \sqrt{\frac{\pi}{a}}$, and integrating over s and s_o gives the following intermediate result:

$$\mathcal{L} = \frac{2 \cdot N_1 N_2 f N_b}{8(\sqrt{\pi})^4 \sigma_x^2 \sigma_y^2} \iint e^{-\frac{x^2}{\sigma_x^2}} e^{-\frac{y^2}{\sigma_y^2}} dx dy. \quad (4.8)$$

Then, integration over x and y gives the widely known expression for the luminosity of two Gaussian beams colliding head-on:

$$\mathcal{L} = \frac{N_1 N_2 f N_b}{4\pi \sigma_x \sigma_y}. \quad (4.9)$$

The more general case does not require equal beams, i.e., $\sigma_{1x} \neq \sigma_{2x}$, $\sigma_{1y} \neq \sigma_{2y}$,

$\sigma_{1s} \neq \sigma_{2s}$ and then Eq. 4.9 becomes:

$$\mathcal{L} = \frac{N_1 N_2 f N_b}{2\pi \sqrt{\sigma_{x1}^2 + \sigma_{x2}^2} \sqrt{\sigma_{y1}^2 + \sigma_{y2}^2}}. \quad (4.10)$$

4.3 Integrated luminosity

As illustrated in the previous section, the instantaneous luminosity that will be called \mathcal{L}' incorporates collider parameters as well as the number of circulating particles in the vacuum chambers. The interaction rate for a specific process is obtained by multiplying this instantaneous luminosity with the cross section which incorporates the physics of the considered interaction. The time integrated value of the instantaneous luminosity [\mathcal{L}'] serves as a measurement of the integrated luminosity expressed as:

$$\mathcal{L}_{int} = \int_0^T \mathcal{L}' dt'. \quad (4.11)$$

The integrated luminosity can be directly related to the number of observed events over the time T:

$$\mathcal{L}_{int} \cdot \sigma = \text{number of events of interest over the time T}. \quad (4.12)$$

One possible solution would be exponential with a given lifetime τ of the beam as expressed in equation 4.13. An exponential decay with time from the start up to the end of the LHC Fill² easily allows an optimization of the instantaneous luminosity as shown in Figure 4.2.

$$\mathcal{L}' = \mathcal{L}_o \exp\left(\frac{-t}{\tau}\right). \quad (4.13)$$

2. Bunches of protons are injected in the LHC and are referred to as fills. Each fill has a number referred to as LHC Fillnumber.

4.4 Luminosity calibration scans

Luminosity monitoring is crucial for the LHC experiments. It is a necessary quantity for every measurement which is performed. The popular method for calibrating the ATLAS luminosity scale is based on the beam displacement technique known as the van der Meer (vdM) scans method (sometimes referred to as beam-separation or luminosity scans) [2]. The main idea of the vdM scans is to measure the effective convolved beams widths in dedicated fills during which the beams are stepwise separated.

The luminosity of a hadron collider can be expressed in terms of the average number of inelastic interactions per bunch crossing (μ), the number of colliding bunch pairs (N_b), the machine revolution frequency (f_r) which is approximately 11 kHz, and the proton-proton (pp) inelastic cross-section (σ_{inel}) as:

$$\mathcal{L} = \frac{\mu N_b f_r}{\sigma_{inel}}. \quad (4.14)$$

The delivered luminosity in ATLAS is monitored by measuring the observed interaction rate per beam crossing (μ_{vis}) using several detectors and various different algorithms for analysis. Therefore, the luminosity is given by:

$$\mathcal{L} = \frac{\mu_{vis} N_b f_r}{\sigma_{vis}}, \quad (4.15)$$

where the visible cross section ($\sigma_{vis} = \varepsilon \sigma_{inel}$) is the total inelastic cross-section multiplied by the detection efficiency ε of a particular detector and algorithm used for analysis. Determining the visible cross-section (σ_{vis}) using the dedicated vdM scans (as explained in [2]) allows an evaluation of the absolute luminosity from direct measurements of the machine and beams parameters. Therefore, the delivered luminosity can be expressed as:

$$\mathcal{L} = \frac{N_b f_r N_1 N_2}{2\pi \Sigma_x \Sigma_y}, \quad (4.16)$$

where N_1 and N_2 are the bunch populations (number of protons per bunch forming the bunch charge product) in beam 1 and beam 2, respectively. Σ_x and Σ_y describe the hori-

zontal (x-scan) and vertical (y-scan) profiles of the colliding beams. During a calibration scan (vdM scan), the beams are separated by steps of known distances that allow a direct measurement of Σ_x and Σ_y .

The quantity depending only on the transverse beam sizes is known as the specific luminosity \mathcal{L}_{spec} that can be extracted from the vdM scan data and can be expressed as [22]:

$$\mathcal{L}_{spec} = \frac{\mathcal{L}}{N_b N_1 N_2} = \frac{f_r}{2\pi \Sigma_x \Sigma_y}. \quad (4.17)$$

4.5 Detectors of luminosity in ATLAS

In addition to the network of MPX detectors, ATLAS has also six separate sub-detectors as described in Figure 4.3 that can be used to measure luminosity. The two main dedicated detectors to monitor the bunch-by-bunch luminosity are LUCID and BCM (Beam Conditions Monitor).

LUCID is a Cerenkov detector that has sixteen mechanically polished aluminum tubes filled with C_4F_{10} gas around the vacuum chamber on each side of the interaction point (IP1) at a distance of 17 m [24] from IP1. BCM consists of four small diamond sensors arranged in a cross pattern on each side surrounding IP1 [25].

The MPX detectors specifically close to the vacuum chamber have proven the capability of providing relative-luminosity measurements during the vdM calibration scans and serving as ATLAS Collaboration cross-check of results obtained with BCM and LUCID. Preliminary results from these MPX luminosity studies for the 2012 data are presented in chapter 5.

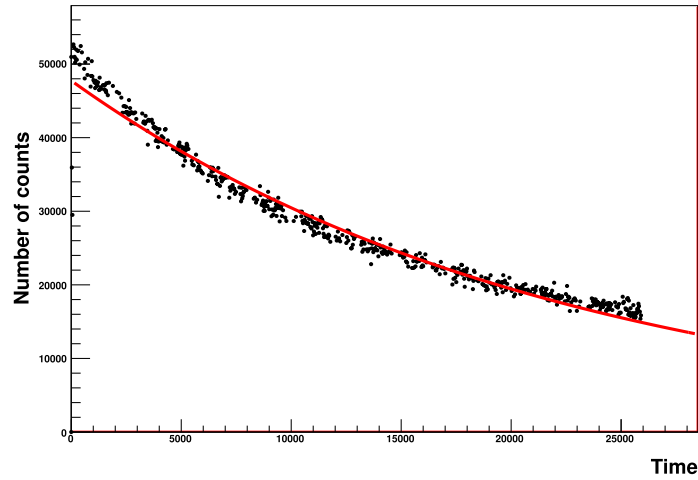


Figure 4.2: Number of counts measured by MPX01 as a function of time [hours] during lead-lead collisions in November 2011. The data is fitted using an exponential fit (see Eq. 4.13).

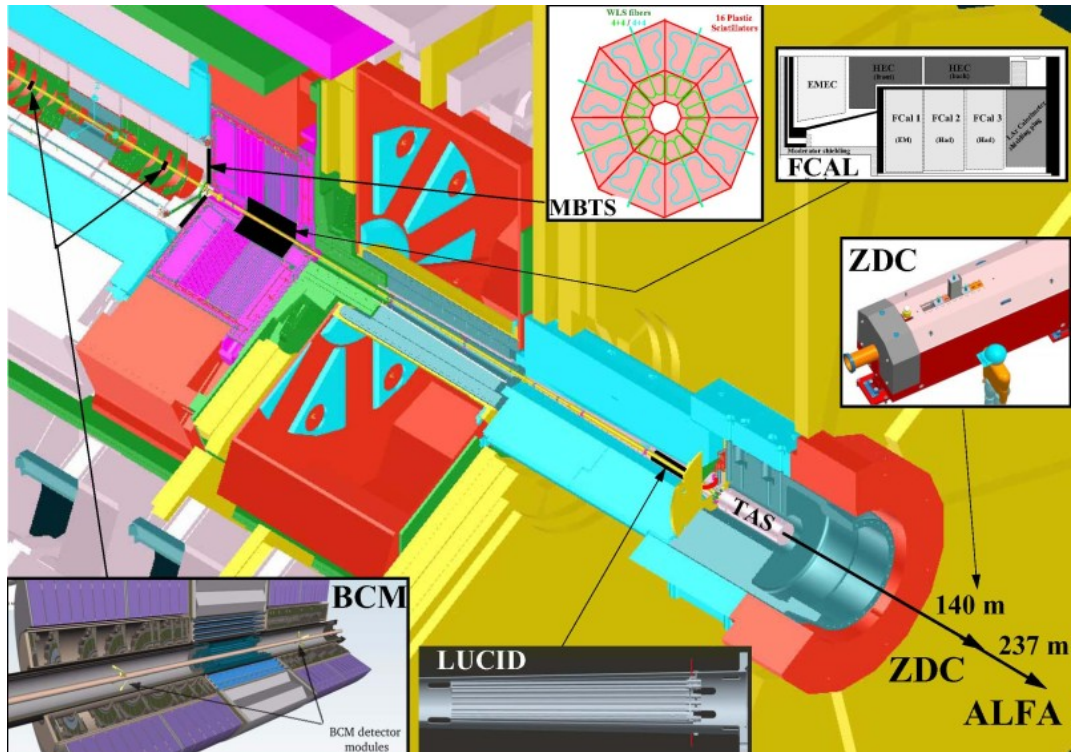


Figure 4.3: Schematic view of the ATLAS detector with dedicated six detectors of luminosity [23] in addition to MPX. The network of MPX detectors also used for luminosity measurements were shown in Figure 3.7

CHAPTER 5

MPX DETECTORS SENSITIVITY TO LHC LUMINOSITY IN 2012

The MPX detectors at different positions give instantaneous measurements of the radiation field at the interaction point in the ATLAS detector allowing the monitoring of the beam movement at any time. Specifically, detectors close to the beam axis can directly be used to monitor the luminosity scans according to the technique of the van der Meer (vdM) beam displacement.

This chapter presents the measurement of the absolute luminosity using the MPX01 detector for the 2012 vdM luminosity calibration scans performed for proton-proton collisions at $\sqrt{s} = 8\text{TeV}$. Only MPX01 was used in this analysis because it is the closest MPX detector to the IP1, and hence have the highest statistics. Moreover, some of the detectors at different positions were damaged by high radiation levels and therefore, they were excluded from this study. The comparison of the ratio of MPX versus BCM luminosity is used to quantify the relative stability of the BCM and MPX luminosity calibrations. Results presented in this chapter have been approved by the ATLAS collaboration and were made public in [1]. In addition, results were presented on behalf of the ATLAS and Medipix2 collaborations in the poster session in the Villa Olmo Conference held at Como, Italy, in September 2013.

5.1 p-p van der Meer luminosity scans

As detailed in chapter 4, the luminosity \mathcal{L} of a hadron collider can be evaluated from the beam parameters as :

$$\mathcal{L} = N_b N_1 N_2 \mathcal{L}_{spec}, \quad (5.1)$$

where

$$\mathcal{L}_{spec} = \frac{f_r}{2\pi\Sigma_x\Sigma_y}. \quad (5.2)$$

The calibration scans at the LHC are performed at a given interaction point, by moving the beams opposing to each other in the two transverse planes, first in the horizontal (x) and then, in the vertical (y) direction. In 2012, the beams were displaced opposing each other by a total of 25 scan steps per plane (horizontal and vertical) giving a full scan range of $\pm 6\sigma_b$ at the IP (σ_b is the nominal beam diameter which was equal to $45 \mu\text{m}$).

The beam orbits at each step are not altered ("quiescent beams") for about 29 s during which the luminosity remains constant. Then, the beams separation is incremented by few tens of microns ("non-quiescent" beams) over a period of several seconds during which the luminosity changes rapidly giving unreliable measurements. Only the data recorded in the time periods when the ATLAS Acquisition Flag¹ = 1, and the beams are not moving, were considered in this analysis.

The MPX exposure time for a frame was set at 5 s with a dead period of about 6 s. Therefore, two frames on average could be recorded within each scan step. From time to time, the MPX devices need to reload their configuration files which could last up to 30 s, causing an absence of some frames; therefore, in some scan steps only one frame is recorded.

The number of counts measured in each frame as a function of the beams separation during the scans in both transverse planes, result in two bell-shaped curves having a maximum corresponding to the maximum rate of collisions at zero beam separation.

During the calibration scans, as a function of the beams separation, a Single Gaussian with a constant background (see Eq. 5.3) and a Double Gaussian with a fixed constant (see Eq. 5.4) are used to fit the horizontal and vertical peaks of the recorded cluster rate. The selection of the fit function depends on the beams shape. However, either method could give the value of the effective horizontal (Σ_x) and vertical (Σ_y) profiles of the colliding beams.

The MPX01 detector was used in the analysis of the three proton-proton vdM scans performed in 2012. It was set at a low threshold of 10 keV and measurements were done in counting mode with exposure time of 5 s. The first scan happened on the 16th of April

1. ATLAS uses a parameter called Acquisition Flag in reference to the beams status; 1 means stable beams, and 0 means unstable beams.

(LHC Fill 2520), while the second scan was done on the 19th of July (LHC Fills 2855, and 2856), and the last scan was performed on the 22nd of November (LHC Fills 3311, and 3316), as shown in figures 5.1, 5.2, and 5.3 respectively.

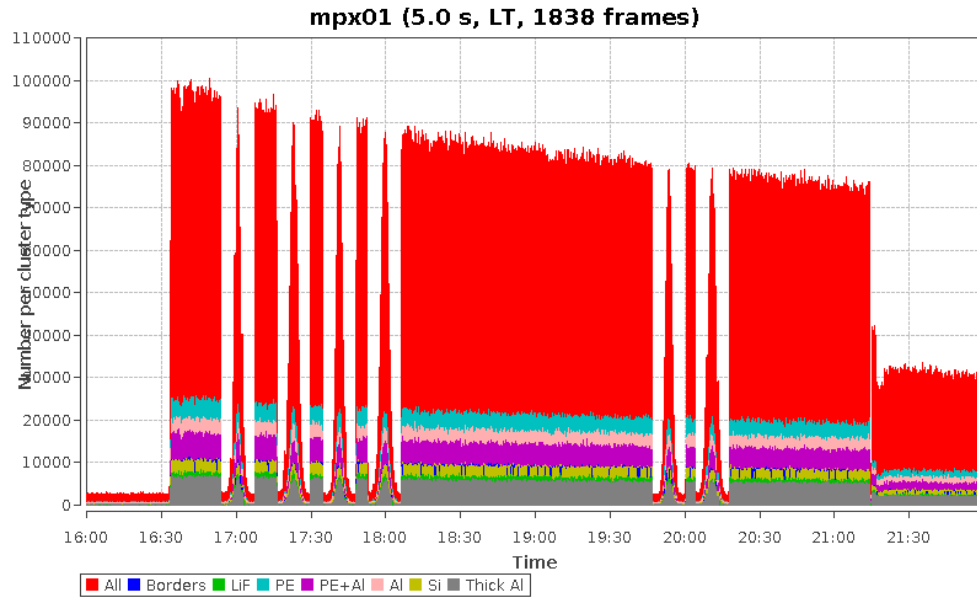


Figure 5.1: van der Meer scans as observed with MPX01 detector with threshold set at 10 keV and exposure time of 5 s in counting mode. A horizontal scan was followed by a vertical scan during LHC Fill 2520 on the 16th of April 2012 (GMT) (see text in section 5.6 for details).

5.2 Noisy pixel removal

Noise due to radiation damage in the electronics or in the silicon layer of the MPX detectors could cause over counting in the pixels. Therefore, the number of events due to noise must be subtracted from the total number of events found in each frame. More specifically, noisy pixels are pixels that have a count rate much higher than the average count rate in a frame. Figure 5.4 shows a frame taken with MPX01 during the vdM scan in November where noisy pixels are marked in red.

Different methods were developed to remove noisy pixels in the analysis and comparison between these methods was reported in [1]. In this analysis, noisy pixel removal is done frame by frame to allow for better filtering of noise; hence, each frame may have

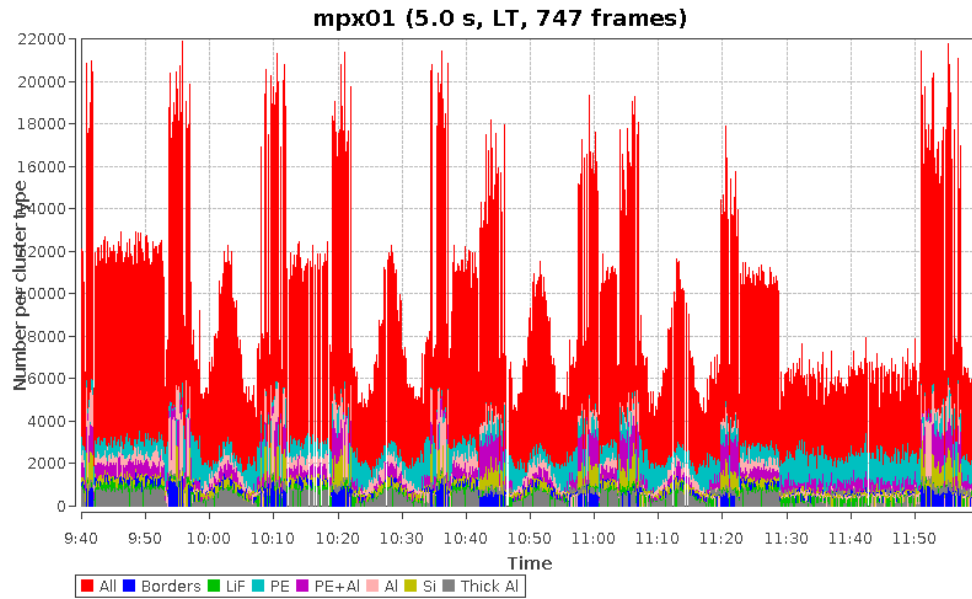


Figure 5.2: Part of the van der Meer scans as observed with MPX01 detector with threshold set at 10 keV and exposure time of 5 s in counting mode. A horizontal scan was followed by a vertical scan during LHC Fills 2855 and 2856 on the 19th of July 2012 (GMT) (see text in section 5.7 for details).

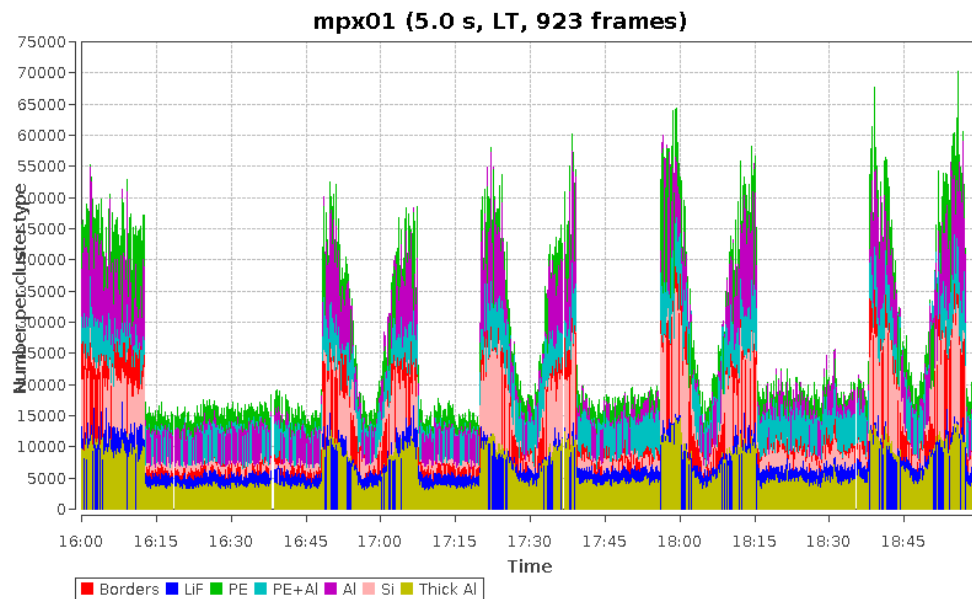


Figure 5.3: Part of the van der Meer scans as observed with MPX01 detector with threshold set at 10 keV and exposure time of 5 s in counting mode. A horizontal scan was followed by a vertical scan during LHC Fills 3311 and 3316 on the 22nd of November 2012 (GMT) (see text in section 5.8 for details).

a different set of noisy pixels removed.

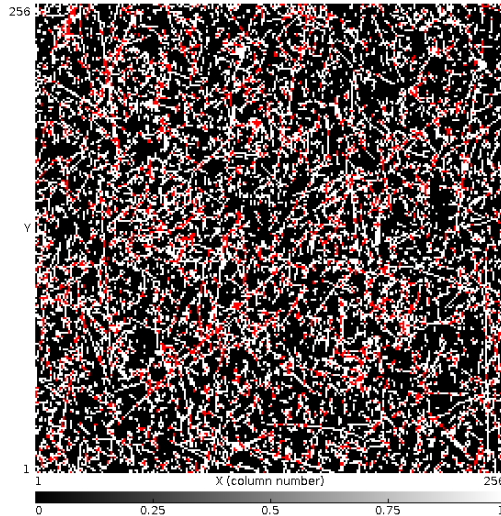


Figure 5.4: A frame taken during the van der Mer scan LHC Fills 3311 and 3316 of November 2012 as observed with MPX01 with threshold set at 10 keV and exposure time of 5 s in counting mode. Noisy pixels are indicated in the frame in red [16].

5.3 Converting counts to luminosity

Luminosity monitoring relies on the measurement of the integrated rate of the interacting particles with the $300\ \mu\text{m}$ thick silicon-sensor of the MPX detectors (counting mode from hit rate measurement). Figure 5.5 shows the number of normalized count rate measured by MPX01 during the first horizontal scan in April as a function of MPX time. The normalization is done with respect to the total number of pixels (65536). The hit rates per frame are converted into luminosity using a normalization factor for each MPX device. This factor corresponds to the integrated luminosity reported by the reference ATLAS luminosity algorithm (BCM V EventOR algorithm [19] using the Beam Conditions Monitor), during an ATLAS run² chosen as a reference (LHC Fill 2649, 21 May 2012) where the ratio of the luminosity reported by MPX01 to the luminosity reported by BCM was equal to 1 as shown in Figure 5.6.

². A run is a period of collisions that might contain more than one LHC Fill.

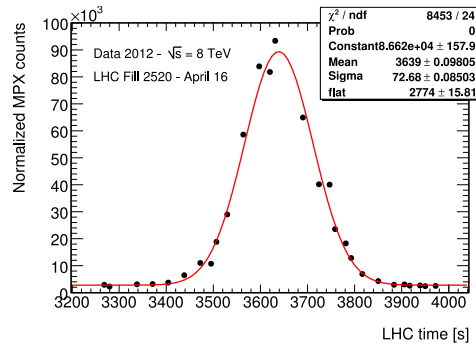


Figure 5.5: The number of normalized count rates measured by MPX01 detector during the first horizontal scan in April (LHC Fill 2520) (see Figure 5.1) as a function of LHC time. The normalization is done with respect to the total number of pixels (65536). The hit rates per frame are converted into luminosity as explained in the text and in Figure 5.6.

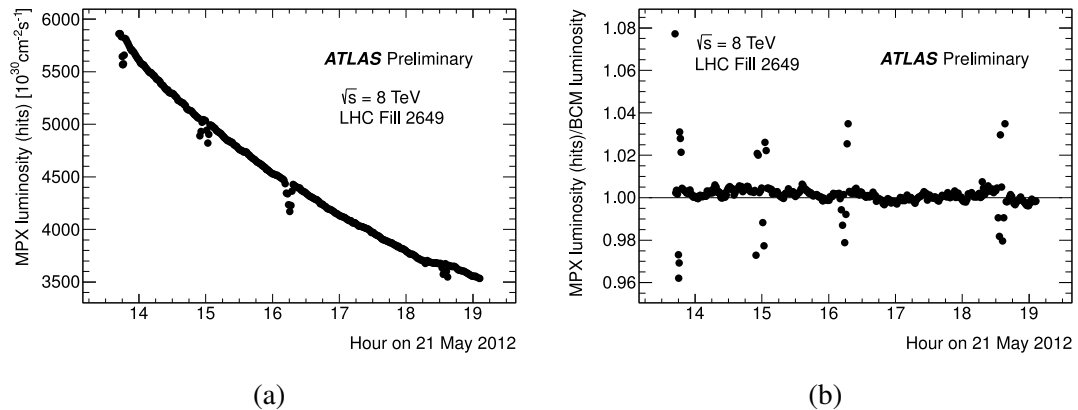


Figure 5.6: Time history of (a) the MPX01 luminosity and (b) the MPX01/BCM luminosity ratio LHC for Fill 2649. The apparent small luminosity dips correspond to times when the LHC operators perform small-amplitude beam-separation scans to optimize the luminosity. During these brief intervals, the luminosity varies more rapidly than can be sampled by the online luminosity and MPX data-taking infrastructure, resulting in unphysical variations of the apparent MPX/ BCM luminosity ratio. This LHC Fill 2646 was chosen as a reference Fill for the analysis of 2012 MPX luminosity data because the MPX01 to BCM luminosity ratio is equal to 1 (see (b)). [1]

5.4 Fitting functions

The data was fitted using two different functions: (i) single Gaussian and a constant term that accounts for instrumental noise and single- beam background, (ii) double Gaussian with a fixed constant term obtained from (i) (the single Gaussian and a constant fit).

A single Gaussian function and a constant is a function of the form:

$$f(x) = Ae^{-\frac{(x-\mu)^2}{2\sigma^2}} + d, \quad (5.3)$$

and has a "bell curve" shape as shown in Figure 5.7. The variables in the above equation are: the amplitude, A , of the curve's peak referred to as the amplitude, the position μ of the center of the peak referred to as the mean, the standard deviation σ that controls the width of the "bell" referred to as sigma, and d is the constant that accounts for the background and referred to as the background.

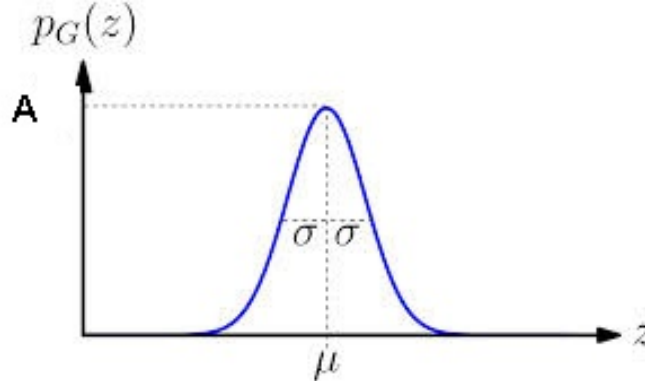


Figure 5.7: A Single Gaussian distribution illustrating a "bell curve" shape with an amplitude A , a mean μ , and a width σ as explained in Eq. 5.3

A double Gaussian function (also referred to as two- dimensional Gaussian function) has the following form:

$$f(x,y) = Aexp\left(-\left(\frac{(x-x_o)^2}{2\sigma_x^2} + \frac{(y-y_o)^2}{2\sigma_y^2}\right)\right) + d, \quad (5.4)$$

where A is the amplitude, x_o, y_o are the mean in x and y directions, σ_x, σ_y are the widths

in x and y directions, and d is a constant.

5.5 Time shift

There was a time shift observed in some luminosity calibration scans in 2012 caused by some reloading or refreshing of the computers connected to the MPX devices. This time shift was observed by comparing the mean obtained from fitting the normalized MPX counts and the luminosity reported by BCM as a function of time. Figure 5.8 shows an example of time shift observed in the April scan LHC Fill 2520. Time shift correction was applied to all the scans in order to insure choosing the right frames for the analysis.

5.6 Results for April scan (LHC Fill 2520)

The April calibration scan was performed on the 16th of April 2012 with LHC Fill 2520 as shown in Figure 5.1. There were six scans; three horizontal numbered as (1X, 2X, and 3X), and 3 vertical scans numbered as (1Y, 2Y, and 3Y) as indicated in Table 5.I. All peaks were fitted using a single Gaussian and a constant term that accounts for instrumental noise and single-beam background. Then, the background obtained from the single Gaussian fit was fixed in the double Gaussian fit giving a better χ^2/ndf as shown in Figure 5.9.

The ratios of the amplitude of MPX01 luminosity to BCM luminosity obtained from the double gaussian fit for all the peaks seen in the April vdM scans are listed in Table 5.I.

The luminosity measured by MPX01 is compared to the luminosity measured by BCM as shown in Figure 5.10, and the data is fitted using a linear form:

$$f(x) = ax + b, \quad (5.5)$$

where a and b are constants. In this case, the constant a is ratio of the luminosity measured by MPX01 to the luminosity measured by BCM, and the constant b accounts for the background.

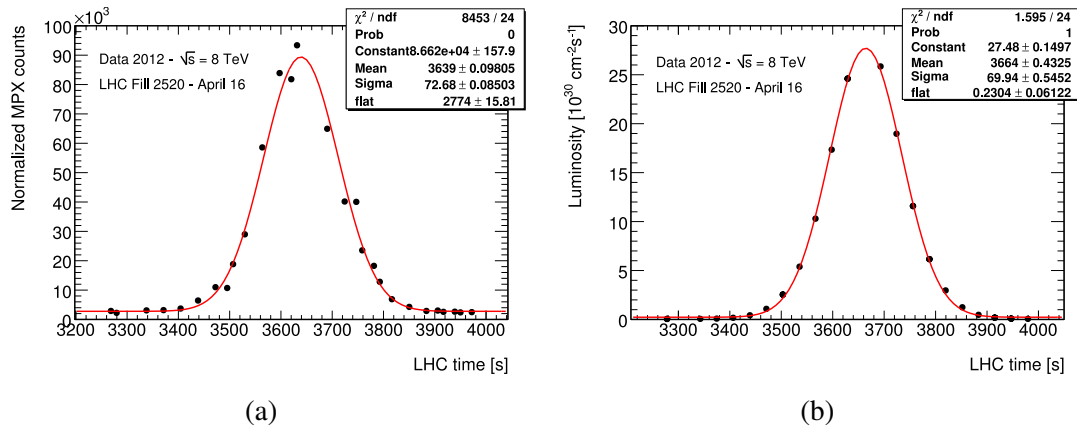


Figure 5.8: Single Gaussian plus constant curve fitted to (a) the count rates measured with MPX01 and to (b) the BCM luminosity as function time during the first horizontal van der Meer scan on the 16th of April LHC Fill 2520. The difference of the mean (the constant b in Eq. 5.3) obtained from the fit reflects a time shift of 25 s.

The background obtained from the single Gaussian plus a constant fit is compared to the background from the linear fit of MPX01 response as a function of the ATLAS reference (BCM) luminosity as listed in Table 5.II for all the scans performed in April. The same analysis was used for the July and November vdM scans.

5.7 Results for July scan (LHC Fill 2855)

The July calibration scan was performed on the 19th of July 2012 with LHC Fills 2855 and 2856 as shown in figure 5.2. There were eight scans; three pairs of horizontal and vertical scans numbered as (4X 4Y, 5X 5Y, and 6X 6Y), one off set³ scan (7X 7Y) and a last pair of a horizontal and vertical scan numbered as (8X 8Y) as indicated in Table 5.III. The same analysis used in April was used in July and results are shown in Figures 5.11, and 5.12. The ratios of the Amplitude of MPX01 luminosity to BCM luminosity obtained from the double Gaussian fit for all the peaks seen in the July vdM scans are listed in table 5.III and the background measured by MPX01 is listed in Table 5.IV.

3. off set scans are performed to determine calibration uncertainties [26]

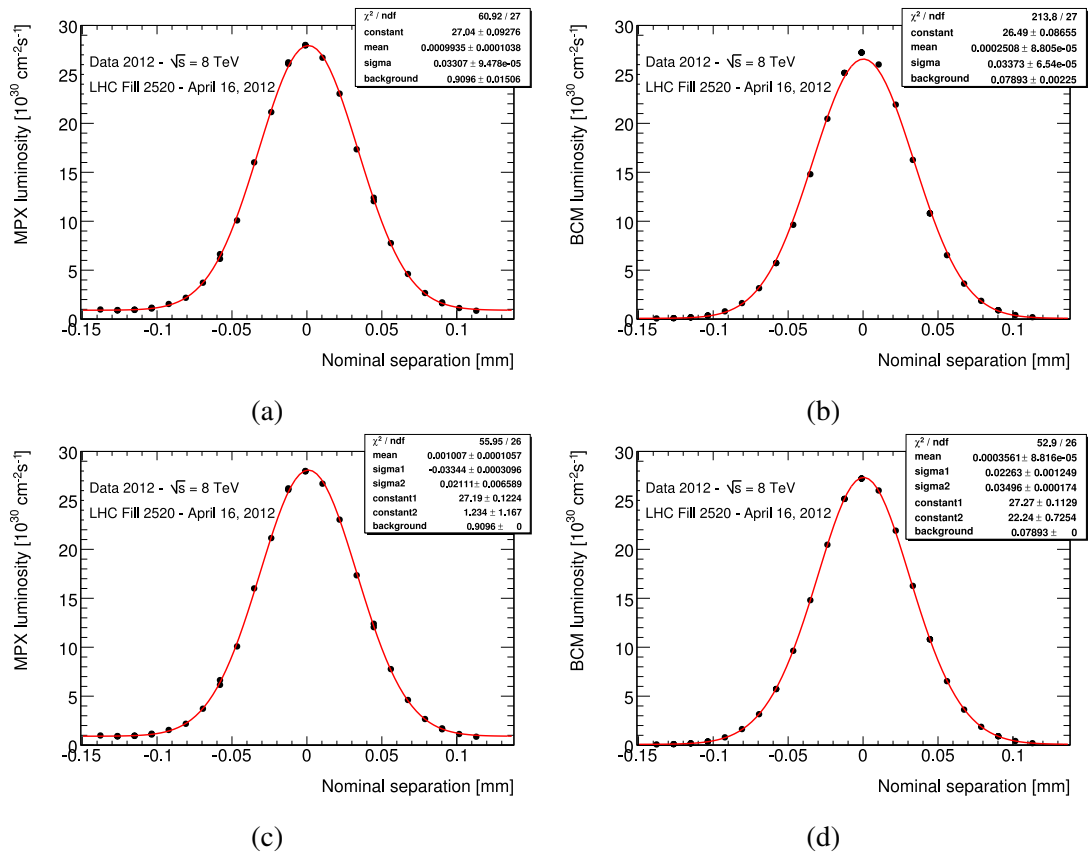


Figure 5.9: The fit function in (a) and (b) is represented in this scan with a single Gaussian and of a constant term that accounts for instrumental noise and single-beam background, where (c) and (d) are well represented by double Gaussian fit with a fixed background obtained from the single Gaussian plus constant fit. (a)-single Gaussian and (c)-double Gaussian are MPX01 hit luminosity during the second vertical April 2012 vdM scan LHC Fill 2520 summed over all bunches as a function of nominal beam separation. Each data point shows the measured instantaneous luminosity before background subtraction and averaged over one sampling interval of the MPX01 device. Because this sampling interval is significantly shorter than the duration of a scan step, and because the MPX data acquisition is not synchronized with the scan, there can be more than one MPX sampling per scan step. The MPX samplings that partially or totally overlap with non-quiet scan steps (varying beam separation) are not shown. (b)-single Gaussian and (d)-double Gaussian, BCM luminosity during the second vertical April 2012 vdM scan summed over all bunches as a function of nominal beam separation. Each data point shows the measured instantaneous luminosity before background subtraction and averaged over the entire duration of a scan step. Data from the scan steps during which the beam separation is varied (non-quiet scan steps) are not shown.

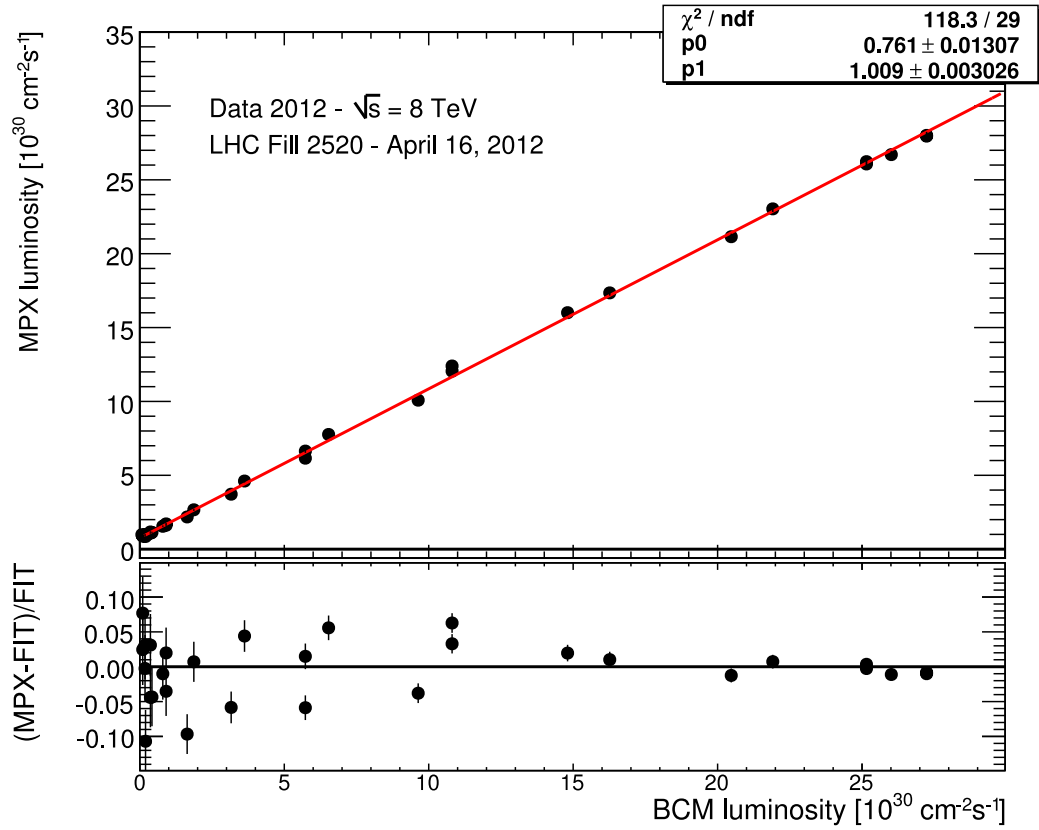


Figure 5.10: MPX01 hit luminosity vs. BCM luminosity for the second vertical April 2012 vdM scan LHC Fill 2520. The line is a linear fit (see Eq. 5.5) to the data. The non-zero intercept corresponds to the difference of the MPX and BCM noise and background contributions. The bottom frame shows the fractional residual of the linear fit.

Table 5.I: Summary of amplitudes [A] of MPX01 luminosity, BCM luminosity and their ratios obtained from the double Gaussian fit of all the scans seen in the April 2012 scan .The statistical error was only considered from the number of counts measured by MPX01 because BCM measurements have much higher statistics.

Peak	MPX01 [A] [$10^{30}\text{cm}^{-2}\text{s}^{-1}$]	Error on MPX01	BCM [A] [$10^{30}\text{cm}^{-2}\text{s}^{-1}$]	Ratio	Error on ratio
1X	28.3	0.141	28.23	1.002	0.005
1Y	27.19	0.122	27.27	0.997	0.005
2X	27.05	0.184	26.83	1.008	0.007
2Y	26.51	0.227	26.26	1.010	0.008
3X	23.73	0.128	23.63	1.004	0.005
3Y	23.88	0.131	23.52	1.015	0.005

Table 5.II: Summary of the background measured by MPX01 obtained from single Gaussian plus a constant fit (Gaussian fit) and the background obtained from the linear fit of MPX01 luminosity versus BCM luminosity (linear fit) of all the scans seen in the April 2012 scan.

Peak	Background (linear fit) [$10^{30}\text{cm}^{-2}\text{s}^{-1}$]	Background (Gaussian fit) [$10^{30}\text{cm}^{-2}\text{s}^{-1}$]	Difference
1X	0.763	0.803	5%
1Y	0.761	0.831	8%
2X	0.718	0.758	5%
2Y	0.735	0.789	7%
3X	0.642	0.667	4%
3Y	0.650	0.701	7%

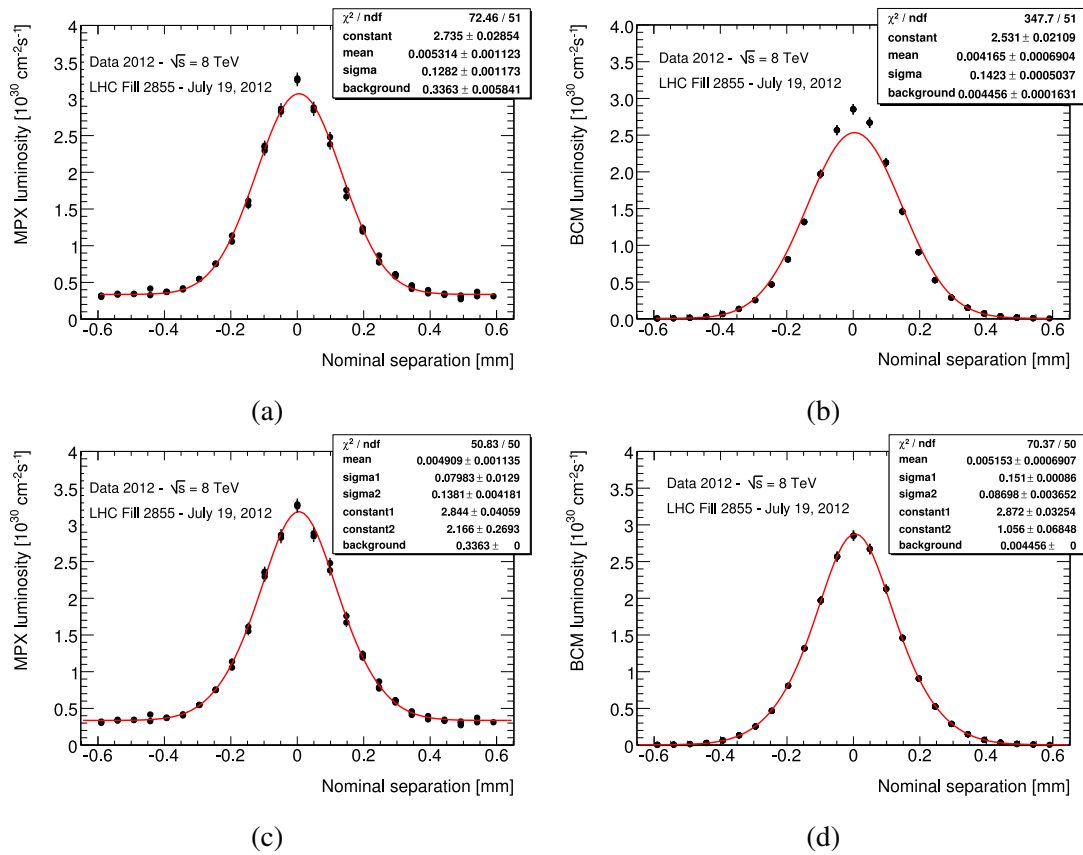


Figure 5.11: The fit function in (a) and (b) is represented in this scan with a single Gaussian and of a constant term that accounts for instrumental noise and single-beam background, where (c) and (d) are well represented by double Gaussian fit with a fixed background obtained from the single Gaussian plus constant fit. (a)-single Gaussian and (c)-double Gaussian MPX01 hit luminosity during the sixth vertical July 2012 vdM scan LHC Fill 2855 summed over all bunches as a function of nominal beam separation. Each data point shows the measured instantaneous luminosity before background subtraction and averaged over one sampling interval of the MPX01 device. Because this sampling interval is significantly shorter than the duration of a scan step, and because the MPX data acquisition is not synchronized with the scan, there can be more than one MPX sampling per scan step. The MPX samplings that partially or totally overlap with non-quiescent scan steps (varying beam separation) are not shown. (b)-single Gaussian and (d)-double Gaussian, BCM luminosity during the sixth July 2012 vdM scan summed over all bunches as a function of nominal beam separation. Each data point shows the measured instantaneous luminosity before background subtraction and averaged over the entire duration of a scan step. Data from the scan steps during which the beam separation is varied (non-quiescent beams) are not shown.

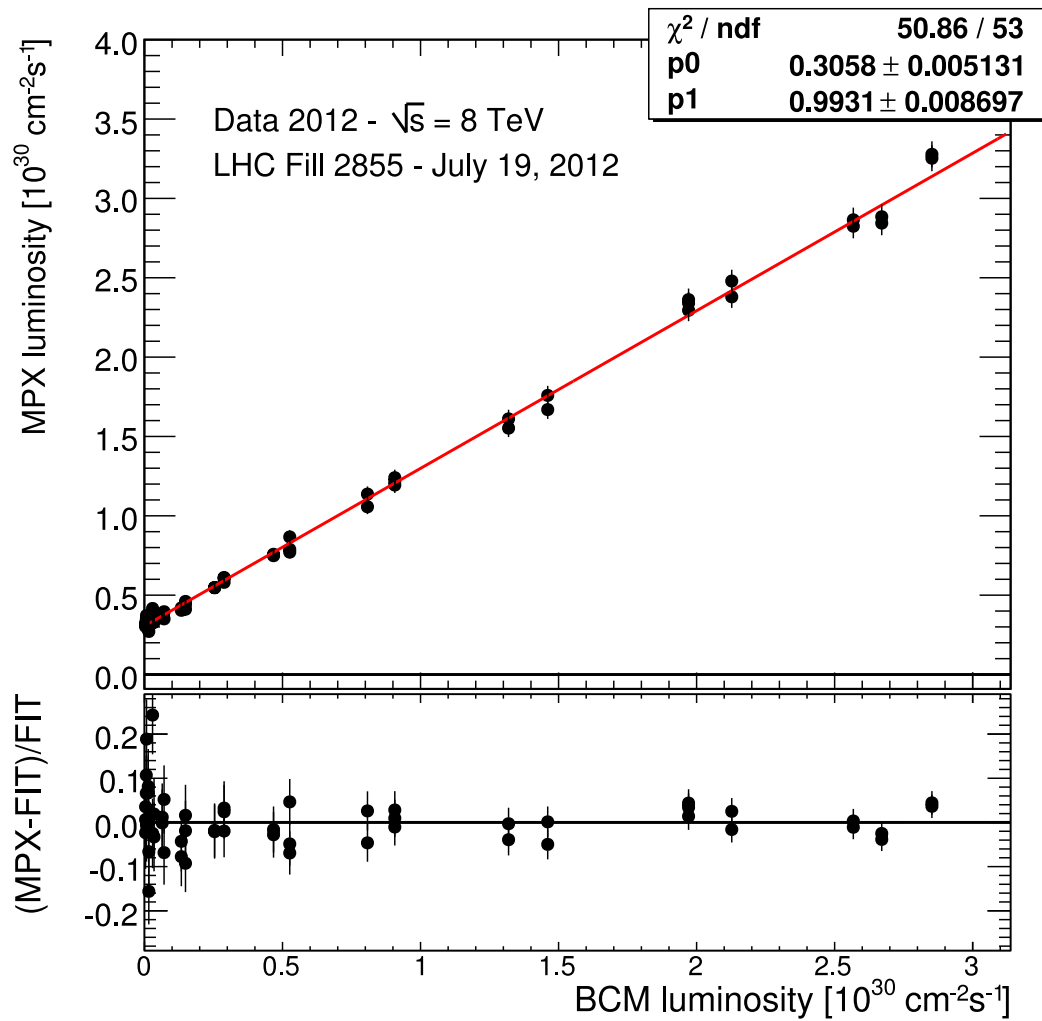


Figure 5.12: MPX01 hit luminosity vs. BCM luminosity for the sixth vertical July 2012 vdM scan LHC Fill 2855. The line is a linear fit (see Eq. 5.5) to the data. The non-zero intercept corresponds to the difference of the MPX01 and BCM noise and background contributions. The bottom frame shows the fractional residual of the linear fit.

Table 5.III: Summary of Amplitudes [A] of MPX01 luminosity, BCM luminosity and their ratios obtained from the double Gaussian fit of all the scans seen in the July 2012 scan. The statistical error was only considered from the number of counts measured by MPX01 because BCM measurements have much higher statistics.

Peak	MPX01 [A] [$10^{30}\text{cm}^{-2}\text{s}^{-1}$]	Error on MPX01	BCM [A] [$10^{30}\text{cm}^{-2}\text{s}^{-1}$]	Ratio	Error on ratio
4X	3.529	0.044	3.492	1.011	0.012
4Y	3.374	0.044	3.388	0.996	0.013
5X	2.957	0.035	3.051	0.969	0.012
5Y	3.000	0.042	2.988	1.004	0.014
6X	2.871	0.032	2.917	0.984	0.011
6Y	2.844	0.041	2.872	0.990	0.014
8X	2.708	0.045	2.766	0.979	0.017
8Y	2.703	0.054	2.710	0.997	0.020

Table 5.IV: Summary of the background measured by MPX01 obtained from single Gaussian plus a constant fit (Gaussian fit) and the background obtained from the linear fit of MPX01 luminosity versus BCM luminosity (linear fit) of all the scans seen in the July 2012 vdM scan.

Peak	Background (linear fit) [$10^{30}\text{cm}^{-2}\text{s}^{-1}$]	Background (Gaussian fit) [$10^{30}\text{cm}^{-2}\text{s}^{-1}$]	Difference
4X	0.336	0.352	5%
4Y	0.336	0.359	7%
5X	0.347	0.354	2%
5Y	0.333	0.358	7%
6X	0.315	0.319	2%
6Y	0.306	0.332	8%
8X	0.279	0.292	4%
8Y	0.288	0.315	9%

5.8 Results for November scan (LHC Fill 3311 and 3316)

The November calibration scan started on the 22nd of November 2012 with LHC Fills 3311 and 3316 as partly shown in figure 5.3. There were eight scans; two pairs of horizontal and vertical scans numbered as (10X 10Y, 11X 11Y), two off set scans (12X 12Y, and 13X 13Y), and two pairs of a horizontal and vertical scan numbered as (14X 14Y, and 15X 15Y) as indicated in Table 5.V. All peaks were analysed with the same approach used in April and July and results are shown in Figures 5.13, and 5.14.

The ratios of the Amplitude of MPX01 luminosity to BCM luminosity obtained from the double Gaussian fit for all the peaks seen in the November vdM scans are listed in Table 5.V, and the background measured by MPX01 is listed in Table 5.VI.

Table 5.V: Summary of Amplitudes [A] of MPX01 luminosity, BCM luminosity and their ratios obtained from the double Gaussian fit of all the scans seen in the November 2012 scan. The statistical error was only considered from the number of counts measured by MPX01 because BCM measurements have much higher statistics.

Peak	MPX01 [A] [$10^{30}\text{cm}^{-2}\text{s}^{-1}$]	Error on MPX01	BCM [A] [$10^{30}\text{cm}^{-2}\text{s}^{-1}$]	Ratio	Error on ratio
10X	2.848	0.059	2.831	1.006	0.021
10Y	2.645	0.041	2.648	0.999	0.015
11X	2.578	0.053	2.632	0.979	0.021
11Y	2.556	0.032	2.556	1.000	0.013
14X	2.411	0.055	2.400	1.005	0.023
14Y	2.301	0.031	2.323	0.991	0.014
15X	2.431	0.030	2.483	0.979	0.013
15Y	2.312	0.029	2.420	0.955	0.013

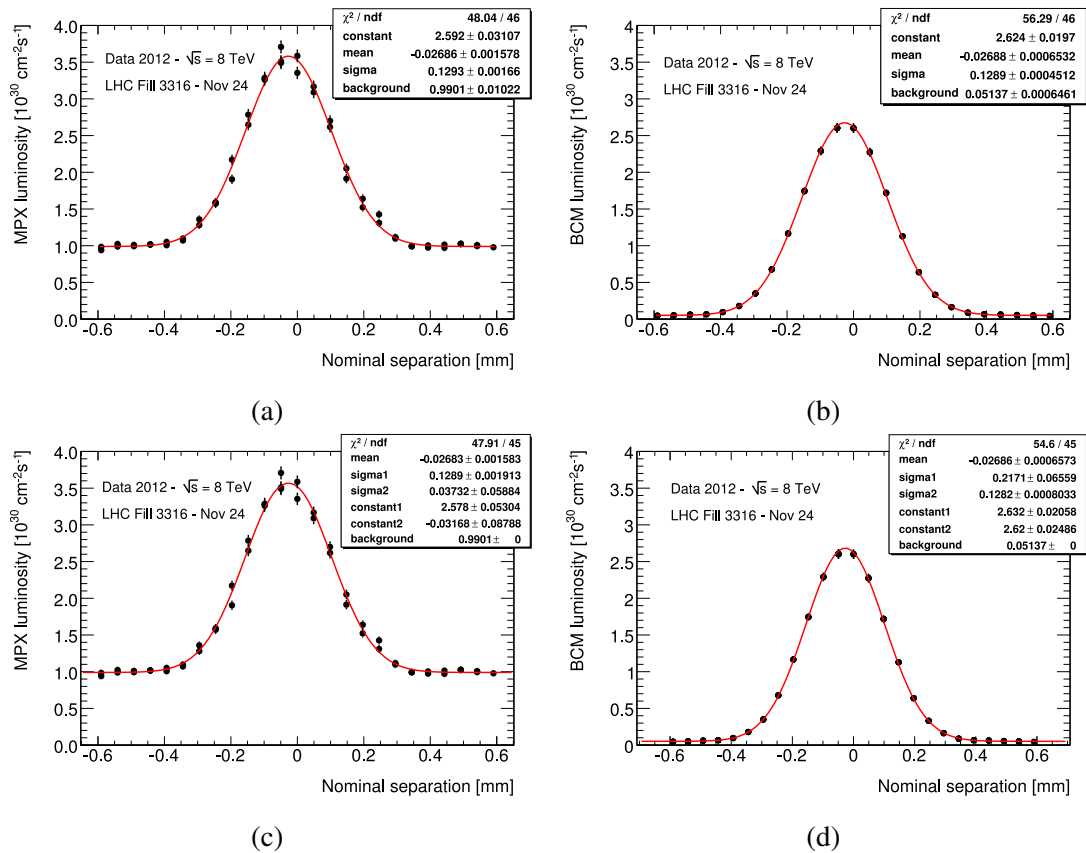


Figure 5.13: The fit function in (a) and (b) is represented in this scan with a single Gaussian and of a constant term that accounts for instrumental noise and single-beam background, where (c) and (d) are well represented with double Gaussian fit with a fixed background obtained from the single Gaussian plus constant fit. (a)-single Gaussian and (c)-double Gaussian MPX01 hit luminosity during the second horizontal November 2012 vdM scan LHC Fill 3316 summed over all bunches as a function of nominal beam separation. Each data point shows the measured instantaneous luminosity before background subtraction and averaged over one sampling interval of the MPX01 device. Because this sampling interval is significantly shorter than the duration of a scan step, and because the MPX data acquisition is not synchronized with the scan, there can be more than one MPX sampling per scan step. The MPX samplings that partially or totally overlap with non-quietescent scan steps (varying beam separation) are not shown. (b)-single Gaussian and (d)-double Gaussian, BCM luminosity during the second horizontal November 2012 vdM scan summed over all bunches as a function of nominal beam separation. Each data point shows the measured instantaneous luminosity before background subtraction and averaged over the entire duration of a scan step. Data from the scan steps during which the beam separation is varied (non-quietescent beams) are not shown.

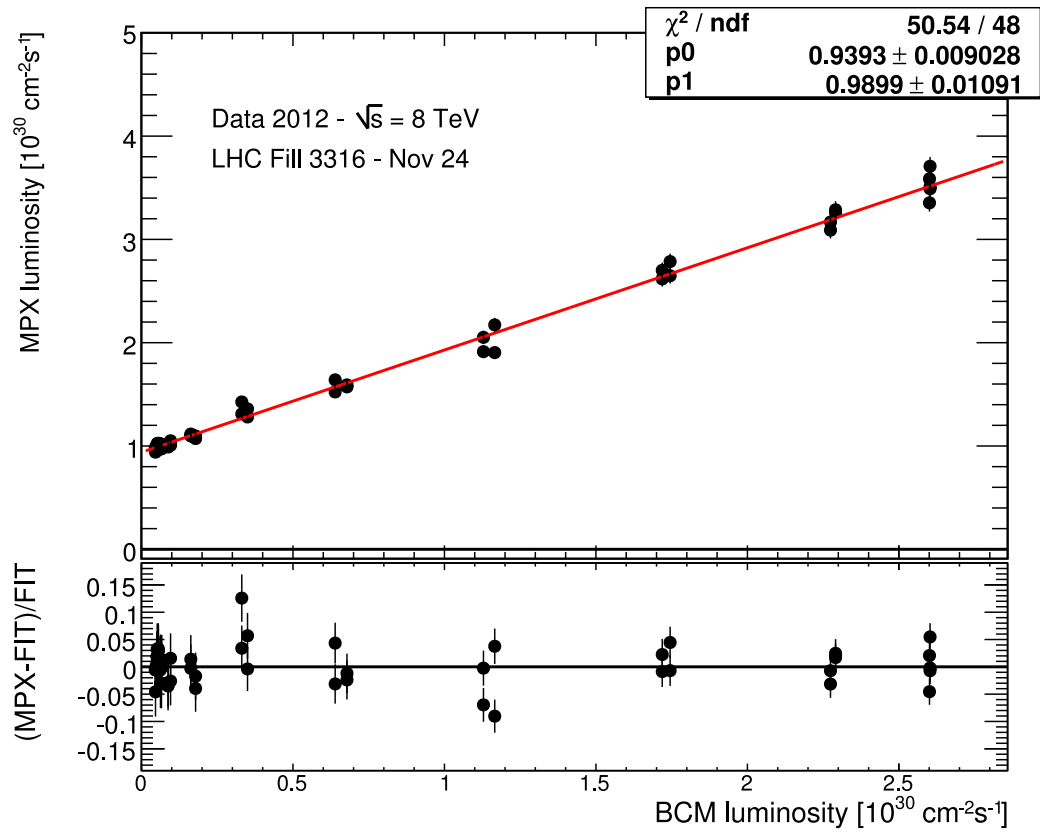


Figure 5.14: MPX01 hit luminosity vs. BCM luminosity for the second horizontal November 2012 vdM scan LHC Fill 3316. The line is a linear fit (see Eq. 5.5) to the data. The non-zero intercept corresponds to the difference of the MPX and BCM noise and background contributions. The bottom frame shows the fractional residual of the linear fit.

Table 5.VI: Summary of the background measured by MPX01 obtained from single Gaussian plus a constant fit (Gaussian fit) and the background obtained from the linear fit of MPX01 luminosity versus BCM luminosity (linear fit) of all the scans seen in the November 2012 vdM scan.

Peak	Background (linear fit) [$10^{30}\text{cm}^{-2}\text{s}^{-1}$]	Background (Gaussian fit) [$10^{30}\text{cm}^{-2}\text{s}^{-1}$]	Difference
10X	0.944	0.951	0.7%
10Y	0.998	1.001	0.9%
11X	0.939	0.939	0.06%
11Y	0.936	0.944	0.8%
14X	0.966	0.953	1.0%
14Y	0.983	0.995	1.0%
15X	0.806	0.813	0.9%
15Y	0.801	0.788	2.0%

5.9 Comparison between luminosity obtained during calibration scans and high luminosity runs

The ratios of the MPX01 luminosity to BCM luminosity obtained during the vdM calibration scans were compared to the ratios obtained during regular runs before and after the vdM scans (high luminosity run). Figure 5.15 is an example of a high luminosity run performed before the vdM scan of November 2012. Ratios from other regular runs before and after the vdM scans in 2012 are listed in Table 5.VII

5.10 Summary of the 2012 vdM luminosity calibration scans

Three vdM calibration scans were performed in 2012. Six scans numbered from 11 to 16 were performed on April the 16th with LHC Fill 2520, eight scans numbered 21 to 28 were performed on July the 19th with LHC Fills 2855 and 2856, and eight scans numbered 31 to 28 were performed on November the 22nd with LHC Fills 3311 and 3316. Figure 5.16 shows the luminosity ratios measured by MPX01 and BCM for all

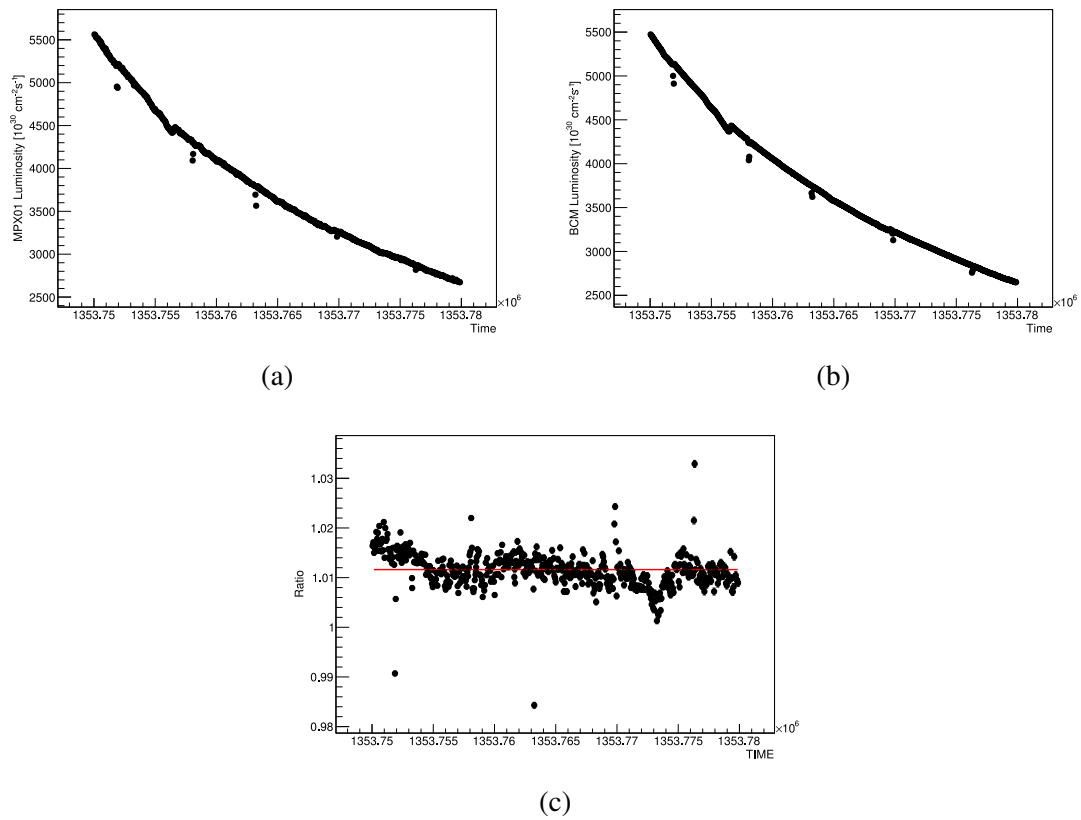


Figure 5.15: High luminosity run performed on the 18th of November 2012. (a) Luminosity measured by MPX01, (b) luminosity measured by BCM, and (c) the luminosity ratio of MPX01 to BCM. The ratio found from the fit is equal to 1.014. The apparent small luminosity dips correspond to times when the LHC operators performed small luminosity optimizations.

Table 5.VII: Summary of ratio of the luminosity measured by MPX01 and BCM for high luminosity runs before and after the 2012 vdM scan. Errors on the ratios are only considered from the number of hits measured by MPX01.

Run date	Luminosity Ratio (MPX01/BCM)	Error
April 15	1.014	0.0002
April 18	1.019	0.0003
July 7	0.988	0.0005
July 21	0.999	0.0002
November 18	1.014	0.0001
November 24	1.011	0.0001

the 22 scans performed in 2012 and the ratios obtained from high luminosity runs before and after the vdM scans.

The ratios had a variation of 1.7%, 4%, and 5%, in the April, July, and November luminosity calibration scans, respectively. The November scans had much more background, almost 65% higher than in July, and 23% higher than in April.

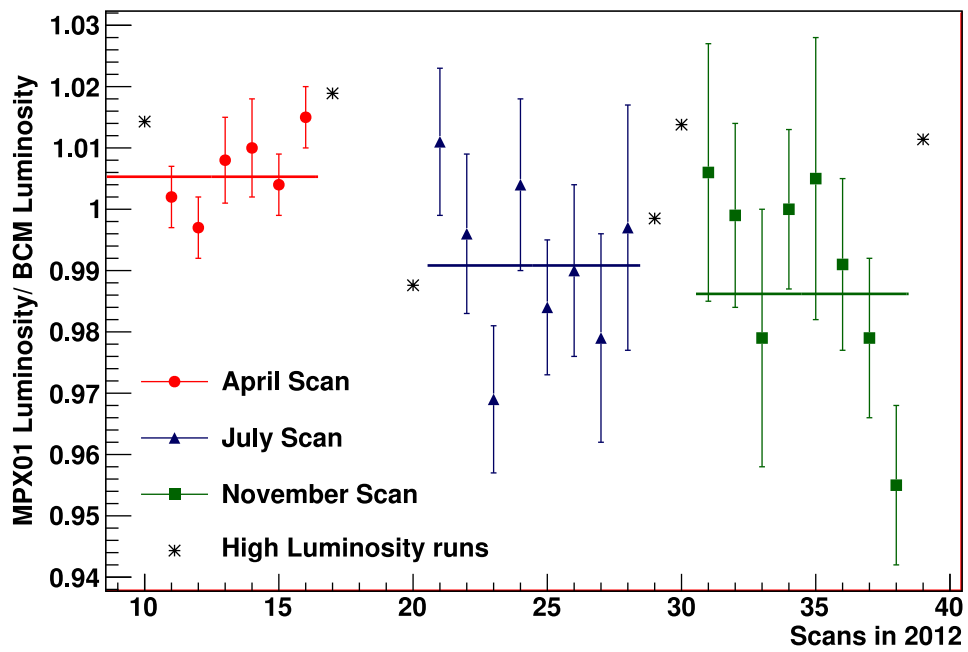


Figure 5.16: Summary of luminosity ratio measured by MPX01 and BCM for the 22 vdM scans performed in 2012 and the luminosity ratio of regular runs before and after the vdM scans. The mean ratio is 1.005 ± 0.002 , 0.991 ± 0.005 , and 0.986 ± 0.005 , for April, July, and November, respectively.

CONCLUSION

The luminosity is the proportionality factor between the number of events generated per second (rate) and the cross section expressing the probability of producing these events. It determines the capability of a particle collider to produce a number of interactions or events. A more precise measurement of the collider luminosity allows a better measurement of cross sections and will have a significant contribution to the investigation of the SM and to new research in physics.

The MPX detectors have successfully operated since 2008 at sixteen different positions in the ATLAS cavern at the LHC. Each detector gives a measure of the radiation field and its spectral characteristics depending on its position with respect to the ATLAS interaction point (IP1). The response of the MPX detectors during collisions was found to be proportional to the LHC proton- proton collisions luminosity⁴. The detectors close to the LHC vacuum chamber and interaction point, such as MPX01, showed a high sensitivity to beams movements at IP1. Therefore, they are able to provide luminosity measurements during the van der Meer (vdM) luminosity calibration scans performed at IP1. This thesis presents the analysis of the three vdM luminosity calibration scans for 2012 proton- proton collisions data taken at the center -of- mass energy of $\sqrt{s} = 8TeV$.

The technique used in the vdM calibration scans consists in moving the beams opposing each other by a definite number of steps in the horizontal and vertical planes at IP1. Two bell- shaped curves (corresponding to the scans in the horizontal and vertical planes) result from the number of counts measured with MPX01 as function of the beams separation during the scans. They were fitted with a single Gaussian and a constant to evaluate the term that accounts for instrumental noise and single beam background. Then, this obtained background was implemented as a fixed constant in a double Gaussian fit. This choice of fit was done to avoid a correlation between a free background and the two Gaussian parameters.

The results obtained with MPX01 were compared to those obtained with BCM (Beam Conditions Monitor). The luminosity measured by MPX01 was found consistent with

4. as reported in [18]

that of BCM within 0.5%, 1%, and 2% for April, July, and November scans, respectively. BCM was chosen for this comparison as it is the luminosity sub-detector of reference chosen by the ATLAS Collaboration. The results obtained from 2012 demonstrate that the MPX detectors can serve as luminosity monitors for ATLAS. Taking into account, the luminosity measurements performed in 2010 and 2011⁵, and the results of the present work, one can conclude that the MPX network gives reliable information for the overall ATLAS luminosity determination over a wide dynamic range (luminosity from $5 \times 10^{29} \text{ cm}^{-2} \text{ s}^{-1}$ up to $7 \times 10^{33} \text{ cm}^{-2} \text{ s}^{-1}$).

5. as also reported in [18]

BIBLIOGRAPHY

- [1] Luminosity Monitoring in ATLAS with MPX Detectors. Technical Report ATLAS-CONF-2013-103, CERN, Geneva, Sep 2013.
- [2] S. van der Meer. Calibration of the effective beam height in the ISR. Technical Report CERN-ISR-PO-68-31. ISR-PO-68-31, CERN, Geneva, 1968.
- [3] ATLAS Public. URL <http://atlas.ch>.
- [4] The ATLAS Collaboration. The ATLAS Experiment at the CERN Large Hadron Collider. *Journal of Instrumentation*, Volume 3:JINST 3 S08003, 2008.
- [5] Irène Vichou. The ACCORDION Calorimetry for LHC. Technical report, LAL Orsay, Université Paris- Sud, 91405 Orsay, FRANCE.
- [6] James R. Chelikowsky and Marvin L. Cohen. Electronic structure of silicon. *Phys. Rev. B*, 10:5095–5107, Dec 1974. doi: 10.1103/PhysRevB.10.5095. URL <http://link.aps.org/doi/10.1103/PhysRevB.10.5095>.
- [7] Simon M. Sze and Kwok K. Ng. Physics of Semiconductor Devices. *WILEY (New York)*, 3rd Edition, 2007.
- [8] L. Tlustos. *Performance and limitations of high granularity single photon processing X-ray imaging detectors*. PhD thesis, Vienna, Tech. U., Vienna, 2005. Presented on 1 Apr 2005.
- [9] P-N Junction. URL <http://hyperphysics.phy-astr.gsu.edu/hbase/solids/pnjun.html>.
- [10] B. Van Zeghbroeck. Principles of Semiconductors Devices. 2011. URL http://ecee.colorado.edu/~bart/book/book/chapter4/ch4_2.htm.
- [11] C. Leroy and P-G Rancoita. Principles of Radiation Interaction in Matter and Detection. *World Scientific (Singapore)*, 3rd Edition, 2012.

- [12] Medipix2 Collaboration. Project Webpage, 2013. URL <http://medipix.web.cern.ch/medipix>.
- [13] M. Filipenko. *Experimental Investigation of Pixelated Semiconductor Photodetectors with CdTe Sensor Material for the Search for the Neutrinoless Double Beta Decay*. PhD thesis, Friedrich-Alexander University, Erlangen, 2011.
- [14] Z. Vykydal. *Microprocessor controlled USB interface for Medipix2 detector*. PhD thesis, Czech Technical University, Prague, 2005.
- [15] D. Turecek, T. Holy, J. Jakubek, S. Pospisil, and Z. Vykydal. Pixelman: a multiplatform data acquisition and processing software package for Medipix2, Timepix and Medipix3 detectors. *Journal of Instrumentation*, 6(01):C01046, 2011.
- [16] Operation page of the ATLAS-MPX network measurements at. URL <http://www.cern.ch/Atlas>.
- [17] J. Bouchami, A. Gutiérrez, A. Houdayer, J. Jakubek, C. Lebel, C. Leroy, J. Macana, J.-P. Martin, M. Platkevic, S. Pospisil, and C. Teyssier. Study of the charge sharing in silicon pixel detector by means of heavy ionizing particles interacting with a Medipix2 device. *Nucl. Instr. and Meth. in phys. Res. A.*, 633, (2011)p.117.
- [18] M. Campbell, E. Heijne, C. Leroy, J-P. Martin, G. Mornacchi, M. Nessi, S. Pospisil, J. Solc, P. Soueid, M. Suk, D. Turecek, and Z. Vykydal. Analysis of the Radiation Field in ATLAS Using 2008 2011 Data from the ATLAS-MPX Network. Technical Report ATL-GEN-PUB-2013-001, CERN, Geneva, Apr 2013.
- [19] Luminosity Determination in pp Collisions at $\sqrt{s} = 7$ TeV using the ATLAS Detector in 2011. Technical Report ATLAS-CONF-2011-116, CERN, Geneva, Aug 2011.
- [20] John Timmer. Following protons on a trip to (and through) the LHC. URL <http://arstechnica.com/science/2010/08/following-protons-on-a-trip-to-and-through-the-lhc/>.

- [21] C. Moeller. General Properties of the Characteristic Matrix in the Theory of Elementary Particles. I. *K. Danske. Vidensk. Selsk. Mat.-Fys. Medd.*, 23(01), 1945.
- [22] Werner Herr and B Muratori. Concept of luminosity. Technical report, 2006.
- [23] The ATLAS luminosity measurement taskforce. URL <http://project-atlas-lucid.web.cern.ch/project-atlas-lucid/taskforce/main.html>.
- [24] The LUCID detector. URL <http://hedberg.web.cern.ch/hedberg/home/lucid/lucid.html>.
- [25] V. Cindro, D. Dobos, I. Dolenc, H. Fraiss-Koelbl, A. Gorisek, E. Griesmayer, H. Kagan, G. Kramberger, B. Macek, I. Mandić, M. Mikuz, M. Niegl, H. Pernegger, D. Tardif, W. Trischuk, P. Weilhammer, and M. Zavrtanik. The ATLAS Beam Conditions Monitor. *Journal of Instrumentation*, 3(02):P02004, 2008. URL <http://stacks.iop.org/1748-0221/3/i=02/a=P02004>.
- [26] The ATLAS Collaboration. Improved luminosity determination in pp collisions at $\sqrt{s} = 7$ TeV using the ATLAS detector at the LHC. *The European Physical Journal C*, 73(8), 2013. ISSN 1434-6044. doi: 10.1140/epjc/s10052-013-2518-3. URL <http://dx.doi.org/10.1140/epjc/s10052-013-2518-3>.